Comparative Study of TESS Photometry and Radial Velocities on Six Early K-type Contact Binaries with Similar Periods around 0.268 Day

N.-P. Liu[1,2] , S.-B. Qian[1,2,3], W.-P. Liao[1,2,3] , Y. Huang[4] , and Z.-L. Yuan[5]

[1] Yunnan Observatories, Chinese Academy of Sciences, P.O. Box 110, Kunming 650216, People's Republic of China; lnp@ynao.ac.cn
[2] Key Laboratory for the Structure and Evolution of Celestial Objects, Chinese Academy of Sciences, P.O. Box 110, Kunming 650216, People's Republic of China
[3] University of Chinese Academy of Sciences, Yuquan Road 19[#], Shijingshan Block, Beijing 100049, People's Republic of China
[4] South-Western Institute for Astronomy Research, Yunnan University, Kunming 650500, People's Republic of China
[5] Department of Physics and Electronics, Hunan Normal University, Changsha 410081, People's Republic of China
Received 2022 May 7; revised 2023 April 21; accepted 2023 April 23; published 2023 May 31

Abstract

High-precision light curves were extracted from TESScut images. Together with APOGEE and LAMOST medium-resolution spectra, a joint study was made for six early K-type contact binary candidates selected unbiasedly with orbital periods around 0.268 day. It is found that all of them (RV CVn, EK Com, V384 Ser, V1038 Her, EH CVn, and CSS_J125403.7+503945) are W-subtype shallow contact systems, though with different mass ratios ($1/q = 0.27$–0.62). The effective temperature differences between the binary components are around a few hundred kelvins. The original definitions of the A and W subtypes were compared with the customarily used methods, which rely on the shape or photometric solutions of the light curves. The latter two methods are not always reliable; therefore, the radial velocity analysis is strongly recommended. Through a collection of all available K-type contact binaries with both photometric and spectroscopic measurements, it is found that almost all of them are W-subtype systems, except for a few objects that have nearly identical temperatures for binary components. This W-subtype phenomenon for K-type contact binaries should be further checked with more samples in the future. Finally, the physical parameters of the targets were determined with joint data analysis, and the multiplicity is discussed for these targets. Objects V384 Ser and RV CVn are confirmed to very likely be triple systems from comprehensive analysis, while V1038 Her is a candidate of a triple system based on photometric and spectroscopic solutions.

Unified Astronomy Thesaurus concepts: Eclipsing binary stars (444); Fundamental parameters of stars (555); Late-type stars (909); Contact binary stars (297); Radial velocity (1332)

Supporting material: machine-readable table

1. Introduction

According to the definition introduced by Binnendijk (1970), late-type (or W UMa–type) contact binaries (CBs) are classified into two classes: A type and W type. We use "subtype" instead of "type," as some new literature has used (Li et al. 2020; Lu et al. 2020; Qian et al. 2020; Alton & Stępień 2021; Li et al. 2021; Panchal & Joshi 2021). For A-subtype contact systems, the more massive component has a higher effective temperature compared to the less massive component, while for W-subtype systems, the less massive component has the higher temperature (Yildiz & Doğan 2013; Li et al. 2021). This definition is more clearly illustrated with radial velocity (RV) variations of real samples. For a W-subtype system (e.g., W UMa), after the primary eclipse (the eclipse when the hotter component is eclipsed), the more massive component is receding from us (redshifted), while the less massive component is moving toward us (blueshifted). Through the analysis of RV curves, it is easy to distinguish which component is the more massive one and thus obtain the subtype configuration.

For totally eclipsing (TE) systems, the definition of A/W classification can be translated into the following criterion based upon the features of the light curves. In A-subtype systems, the deeper minimum is caused by the transit, while in

W-subtype systems, it is caused by the occultation of the less massive component (Latković et al. 2021). However, not all CBs are TE systems. Partially eclipsing (PE) systems are more common. Meanwhile, even for TE systems, the task of classifying the A and W subtypes becomes challenging when the light curves have comparable depth at the transit and occultation phases. A good example is 1SWASP J064501.21 +342154.9 (hereafter J0645). Liu et al. (2014a) classified this system to be W-subtype according to the photometric solutions based on the original definition. Then, a later study (Djurašević et al. 2016) reclassified it to be A-subtype by relying only on the transit occultation feature of the light curves, but in fact, their photometric solutions also support the W-subtype configuration. This ambiguity in classifying the subtypes occurs because the transit and occultation of the light curves have almost identical depths. The slightly shallow occultation is actually the eclipse of the hotter component. A similar feature is shown in the case of TYC 01664-0110-1 (Alton & Stępień 2016).

On the other side, there are more PE systems that cannot be classified using the criterion above. Photometric solution is therefore the fundamental tool. However, it is just the PE systems whose photometric solutions may have large errors (Hambálek & Pribulla 2013; Li et al. 2021; Liu 2021). Their mass ratios are even thought to be unreliable (Hambálek & Pribulla 2013; Latković et al. 2021), especially for asymmetric light curves (in other words, spotted systems). The mass ratios derived from spectroscopic studies may be different from those

based on photometric analysis (e.g., Rucinski et al. 2000; Yakut & Eggleton 2005). Therefore, RV measurements are very important for determining accurate physical parameters and verifying the reliability of the photometric approach. However, there were only a few late-type CBs (especially those later than G-type) studied with RV data (e.g., i Boo, Hill et al. 1989; SW Lac, Zhai & Lu 1989) until an RV program from the David Dunlap Observatory (DDO) in Toronto (hereafter the DDO program) started. This program lasted for almost 10 yr, and a series of papers was published (e.g., Lu & Rucinski 1999; Rucinski 2002; Pribulla et al. 2009) that has greatly increased the samples of late-type CBs with RV data. Among those CBs, the K-type systems have the shortest periods, which are close to the period cutoff (~0.22 day) according to the period–color relation (Eggen 1967; Rucinski 2002). From their RV data, it is inferred that almost all of the K-type CBs are W-subtype systems (see Section 4). This result is quite different from the overall statistical result of the late-type CBs, most of which are from photometric studies, that no significant difference in numbers is found for A and W subtypes. Yildiz & Doğan (2013) reported that among 100 well-studied CBs, there are 51 A subtypes and 49 W subtypes. Recent statistical studies of CBs also show a similar result (e.g., Sun et al. 2020; Latković et al. 2021; Li et al. 2021). Even for CBs with ultrashort periods, a recent statistic work found a nearly equal number of W- and A-subtype systems (Li et al. 2019).

So far, the A- and W-subtype classification has been widely used in the study of late-type CBs, not only in the statistic research (e.g., Sun et al. 2020; Latković et al. 2021) but also for the formation and evolution science (e.g., Yildiz & Doğan 2013; Yıldız 2014). Therefore, it is important to get the correct subtype configuration. However, the difference between the spectroscopic and photometric statistic results in the W and A subtypes is noticeable, particularly in K-type targets. The problem is that the samples of K-type CBs with RV data are not numerous enough. Thanks to the era of large surveys, we could collect data from both photometric and spectroscopic surveys, including the foregoing Kepler mission (Borucki et al. 2010; Koch et al. 2010) and the present Transiting Exoplanet Survey Satellite (TESS; Ricker et al. 2015) for the photometric part and Sloan Digital Sky Survey (SDSS; Eisenstein et al. 2011; Abolfathi et al. 2018) and Large Sky Area Multi-Object Fiber Spectroscopic Telescope (LAMOST; e.g., Cui et al. 2012; Zhao et al. 2012) for the spectroscopic part. In the present study, we mainly utilized data from TESS and the Apache Point Observatory Galactic Evolution Experiment (APOGEE; Majewski et al. 2017).

TESS is currently one of the most important ongoing all-sky projects, which initially plans to measure the brightness of ~200,000−400,000 selected stars at a 2 minute cadence; simultaneously, the full-frame images (FFIs) are obtained at a 30 minute cadence (Stassun et al. 2018). It conducts a sequential set of 27.4 day photometric lsurveys of $24° \times 96°$ sky sectors and results in observations of 80%–85% of the sky (Feinstein et al. 2019; Nardiello et al. 2019) every 2 yr with a photometric precision of about 60 ppm to 3% for stars brighter than $T_{mag} \approx 16$ (Oelkers & Stassun 2018). This project is intentionally designed for exoplanet detection, which, however, extremely facilitates the research of eclipsing binaries (e.g., Lee et al. 2019; Borkovits et al. 2020). Except for the light curves from short cadences (1 or 2 minute exposures) for selected targets, the FFIs of TESS provide a huge data-mining archive

for scientific research of diverse objects. The light curves used in this study are mostly from this archive.

APOGEE is a large near-infrared (NIR) spectroscopic survey launched within SDSS-III (Eisenstein et al. 2011) and later continued in SDSS-IV (Blanton et al. 2017). APOGEE has produced a large collection of high-resolution ($R = 22,500$), high-quality (S/N >100) infrared (H-band) spectra for stars throughout the Milky Way (Majewski et al. 2016). APOGEE affords us more than half a million spectra of some 150,000 stars (APOGEE-1), which is an ideal resource for spectroscopic study. However, because of its NIR band and the spectral line entanglement problem for close binaries, this treasure was not paid enough attention for the research of short-period close binaries, until recently. Jayasinghe et al. (2020) combined APOGEE with other databases to study CBs. Clark Cunningham et al. (2019) used APOGEE spectra to measure RVs of close binaries with long periods, which they applied a broadening function technique (Rucinski 2002) to accomplish. By utilizing the APOGEE spectra together with the high-precision space TESS photometric data, it is hoped that joint studies can be made of K-type CBs that provide evidence for the A/W-subtype problem.

This paper is structured as follows. The light-curve extraction and data analysis are introduced in Section 2. The results for individual targets are presented in Section 3. We summarize and discuss our results in Section 4.

2. Data Method

2.1. Target Selection

We tried to select a few early K-type CBs through cross-matching the APOGEE catalog with the VSX database (Watson et al. 2006). Candidates were then checked using the TESS images (within cycle 2 of the TESS mission). The final targets were selected based on the following criteria.

1. Periods within the range of 0.26–0.27 day.
2. Not too faint; the magnitude in the V band is brighter than 14.5.
3. Variation amplitude not too low; amplitudes in the V or R bands are larger than 0.08 mag.
4. Enough spectroscopic observations, at least three to five visit spectra. If not enough, try to collect additional observations from LAMOST.
5. Available observations with TESS.
6. No bright companions in the close field within a distance of 5 TESS pixels (1 pixel = 21″).

These criteria ensure effective data for the present study; meanwhile, they should not have a selection effect on the subtype problem. It is worth mentioning that for the first criterion, the motivation is that too-short periods will cause a more serious smear effect. In addition, 0.26–0.27 day is approximately the longest period for K-type CBs. Finally, we collected the six targets selected in this study: RV CVn, EK Com, and V384 Ser in group I and V1038 Her, EH CVn, and CSS_J125403.7+503945 (hereafter J125403) in group II. The group labels are only for convenience. Their basic information is listed in Table 1.

2.2. Light Curves from TESS

Our targets were observed by TESS in the cycle 2 period, which is the first year of its north-sky phase. The images were

<div align="center">

Table 1
Basic Information for the Variables from the Databases

</div>

Name	α_{2000}	δ_{2000}	V mag	Period (days)	$J - H$	$T_{\rm eff}$ (K)[a]	Sp. Type[b]	plx (mas)[a]	plxe (mas)[a]	Sector[c]
RV CVn	13 40 18.16	+28 18 21.5	13.84	0.269567	0.567	4853	⋯	2.346 ± 0.022	2.408 ± 0.019	23
EK Com	12 51 21.44	+27 13 47.0	12.166	0.266685	0.444	4958	G8–G9	5.105 ± 0.052	5.164 ± 0.018	23
V384 Ser	16 01 53.57	+24 52 17.5	11.88	0.268729	0.476	4879	K2	4.701 ± 0.037	5.039 ± 0.056	24, 25
V1038 Her	16 58 19.78	+33 40 21.6	11.90	0.2681798	0.539	4837	K3	5.454 ± 0.134	5.492 ± 0.066	25
EH CVn	13 41 13.70	+31 47 24.3	13.00	0.2635829	0.522	5045	K3–K5	3.697 ± 0.029	3.734 ± 0.014	23
J125403	12 54 03.61	+50 39 45.9	14.30	0.268798	0.430	4904	⋯	1.590 ± 0.020	1.604 ± 0.016	15, 16

Notes.
[a] Retrieved from Gaia DR2 (Gaia Collaboration et al. 2018) and EDR3 (Gaia Collaboration et al. 2021; Lindegren et al. 2021).
[b] From LAMOST LRS.
[c] TESS sector.

taken with a 30 minute cadence. The TESS FFI cutouts (TESScut[6]; Brasseur et al. 2019) for each target were downloaded from the service of the Mikulski Archive for Space Telescopes (MAST)[7] with the help of the lightkurve package (Lightkurve Collaboration 2018). The cutouts have sizes of 10×10 to 13×13 pixels, depending on each target. Similar to Guo et al. (2020), the apertures and background masks from a master image were created using a percentile thresholding method and used to generate light curves. Usually, for the raw light curves, we need to remove the low-frequency trend using a polynomial fitting method and remove the data with anomalies (various spacecraft anomalies, thermal transient characteristics, differential velocity aberration, artifacts, etc.). The final master images and the apertures of target group I are shown in Figure 1, together with the extracted light curve of RV CVn (without detrending) as an example.

2.3. Photometric Solutions

The TESS light curves of the targets turn out to be of good quality, with small errors (mostly 0.001–0.002, occasionally 0.003–0.004 mag) after removing a few outliers. Good precision is favorable for determining accurate photometric solutions (Liu 2021). To get the photometric solutions, the light curves were analyzed using the Wilson–Devinney (W-D) code (Wilson & Devinney 1971; Wilson 1979, 1990, 1994; Van Hamme & 2007; Wilson 2008; Wilson et al. 2010; Wilson 2012) version 2013. This version not only enables the automatic calculation of limb-darkening coefficients but can also deal with light curves with long time exposures, which may cause notable smear effects. This is very useful for the long-cadence TESScut light curves of short-period CBs (typically ∼0.3 day). Therefore, we incorporated the W-D code into Python scripts in order to make it more convenient to work with, especially in the grid search process (e.g., the q-search).

In order to make a comparative study, photometric solutions were initially derived independently of the RVs. The calculation was carried out following a common procedure (e.g., Liu et al. 2020). The temperature of one component was fixed, while that of the other component was set free. The solutions were searched at a series of fixed mass ratios ($q = m_2/m_1$), which is the so-called q-search method (e.g., Qian et al. 2005). Before calculation, mode 3 (contact model) was initially assumed. The gravity-darkening coefficients were set as
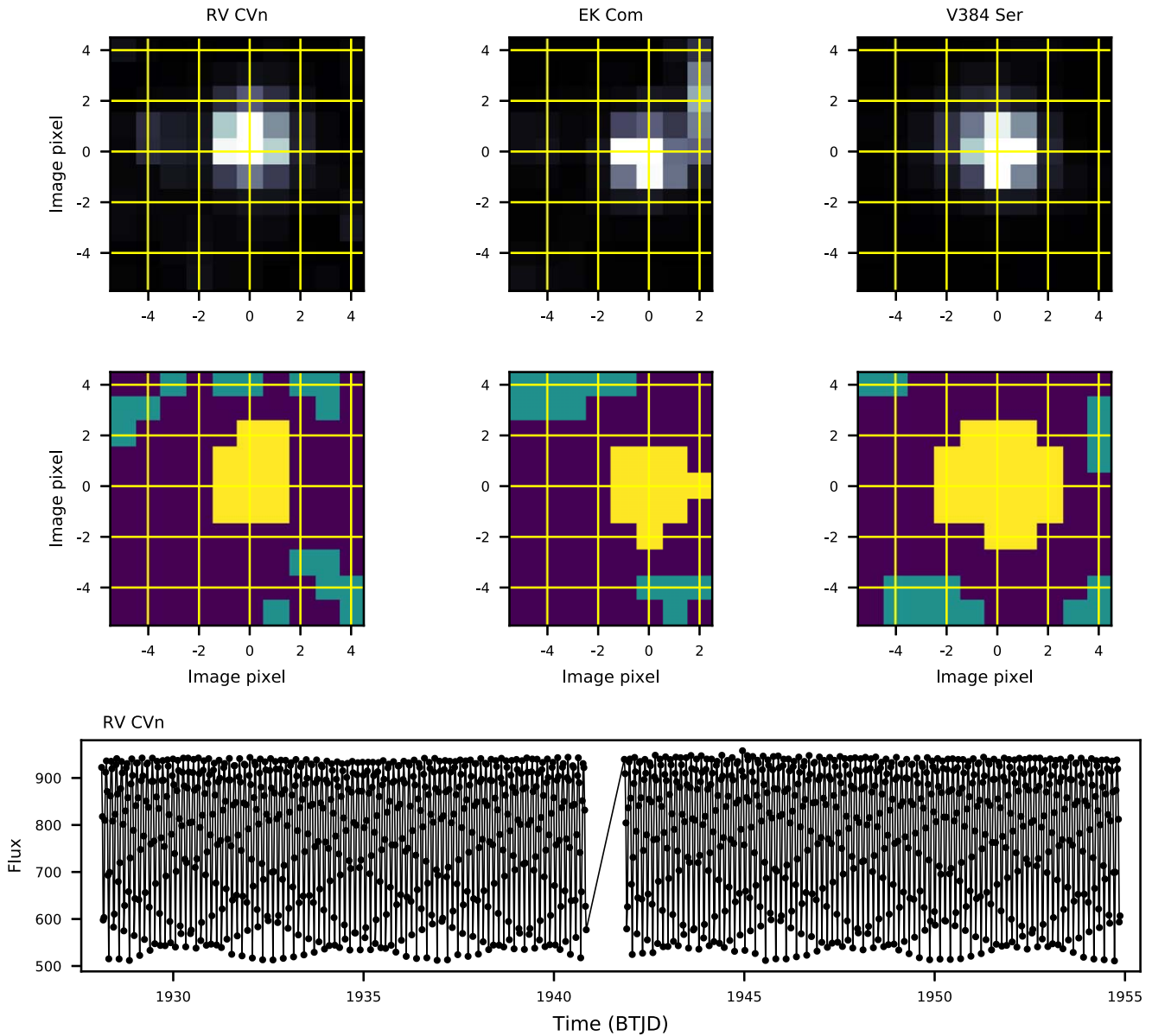
$g_1 = g_2 = 0.32$ (Lucy 1967), and the bolometric albedo was set as $A_1 = A_2 = 0.5$ (Ruciński 1969) according to their low temperature. The square-root functions (LD = −3) were chosen for the treatment of limb-darkening. The limb-darkening coefficients in the band of "TESS" were used (the coefficient files were kindly provided by Professor Van Hamme) and interpolated in the W-D code. The NGA (the number of abscissae) was set to 3 to account for the smear effect (Wilson 2012; Zola et al. 2017). After the q-search was done, the achieved mass ratio was used as an initial input for comprehensive solutions (Liu et al. 2020). In the final calculation, the parameter of the third light should be set free, because for TESS light curves, there might be blending of light from nearby stars (Guo et al. 2020). The q-search diagrams are shown in the left panels of Figures 2 and 3, while the observed and theoretical light curves are displayed in the corresponding right panels. The photometric solutions are shown in Tables 2 and 3. The errors listed in parentheses are the standard deviations directly calculated by the W-D code, which, for the nonlinear situations, are not ideally correct. The real uncertainties may be three or five times larger, depending on the confidence level (Liu et al. 2015). The main characteristics of each set of photometric solutions are labeled in the head of the corresponding column. For asymmetric light curves, cool or hot spots were modeled in the calculation. Parameters of spots include the latitude θ, longitude ψ, radius r, and temperature factor T_s/T_*. They are also listed in the tables together with the spot location (on which star). Some detailed explanations of calculation and analysis for individual targets are presented in Section 3.

2.4. RV Studies

Photometric solutions derived merely from light curves may not always be reliable (see Section 1). To check the photometric results, we utilized the spectra from APOGEE (Majewski et al. 2017), as well as a few spectra from the LAMOST medium-resolution survey (MRS; Liu et al. 2019; Wang et al. 2019; Liu et al. 2020). The MRS spectra cover two wavelength bands: 495–535 and 630–680 nm for the so-called blue (B band) and red (R band) bands, respectively (Zong et al. 2018; Wang et al. 2019). In this data set, they are usually observed for three continuous short exposures. In order to avoid the Hα region (activity problem; see, e.g., Liu et al. 2020), only spectra in the B band were used for RV determination. For APOGEE spectra, the data used in this paper were retrieved from SDSS DR14 and DR16. The latest description of the APOGEE data can be found in

---

[6] https://mast.stsci.edu/tesscut/
[7] https://mast.stsci.edu/portal/Mashup/Clients/Mast/Portal.html

Figure 1. Aperture photometry of the targets. The top and middle panels show the observed images and the corresponding apertures (yellow for the aperture and blue for the background), respectively. The extracted light curve of RV CVn is shown in the bottom panel.

Jönsson et al. (2020). Some information on the targets retrieved from the APOGEE and LAMOST databases are listed in Tables 4 and 5, respectively.

We implemented the traditional cross-correlation function (CCF) method (Szalai et al. 2007; Matijevič et al. 2010) to measure the RVs. For the APOGEE spectra, the data utilized are the individual visit spectra (apVisit). To calculate the CCFs, the sharp features (mostly fake emission and absorption) in narrow windows (usually less than 2 or 3 pixels) were first removed to get the clean spectra. They were then normalized by fitting the continuum using a Chebyshev polynomial. The normalized spectra of RV CVn from SDSS DR14 are displayed in Figure 4 as an example. The CCFs were calculated by cross-correlating the normalized spectra with a standard template (NGC 5272 17) that was selected from the new catalog of RV standard stars (Huang et al. 2018). The CCF images are displayed in Figures A1–A3, and the results are shown in Tables 4–6. Finally, the RV data were fitted (Figure 5) using

the W-D code, taking into account the eclipse and proximity correction (Baran et al. 2004; Wilson 2008) for the binary components. The value of the semimajor axis was set free during the calculation, and the absolute physical parameters were derived accordingly. The results are listed in Table 9. More details about the RV calculation are addressed in the following section.

3. Results

3.1. RV CVn

The variability of RV CVn has been known for almost a century, since its first discovery by Larink (1921). It has been subsequently studied by several authors (e.g., Schilt 1927; Hoffmann 1981; Liu et al. 2014; Zasche et al. 2014), and two sets of photometric solutions were recently published. However, their solutions are quite different. The mass ratios from Liu et al. (2014) and Zasche et al. (2014) are 1.74
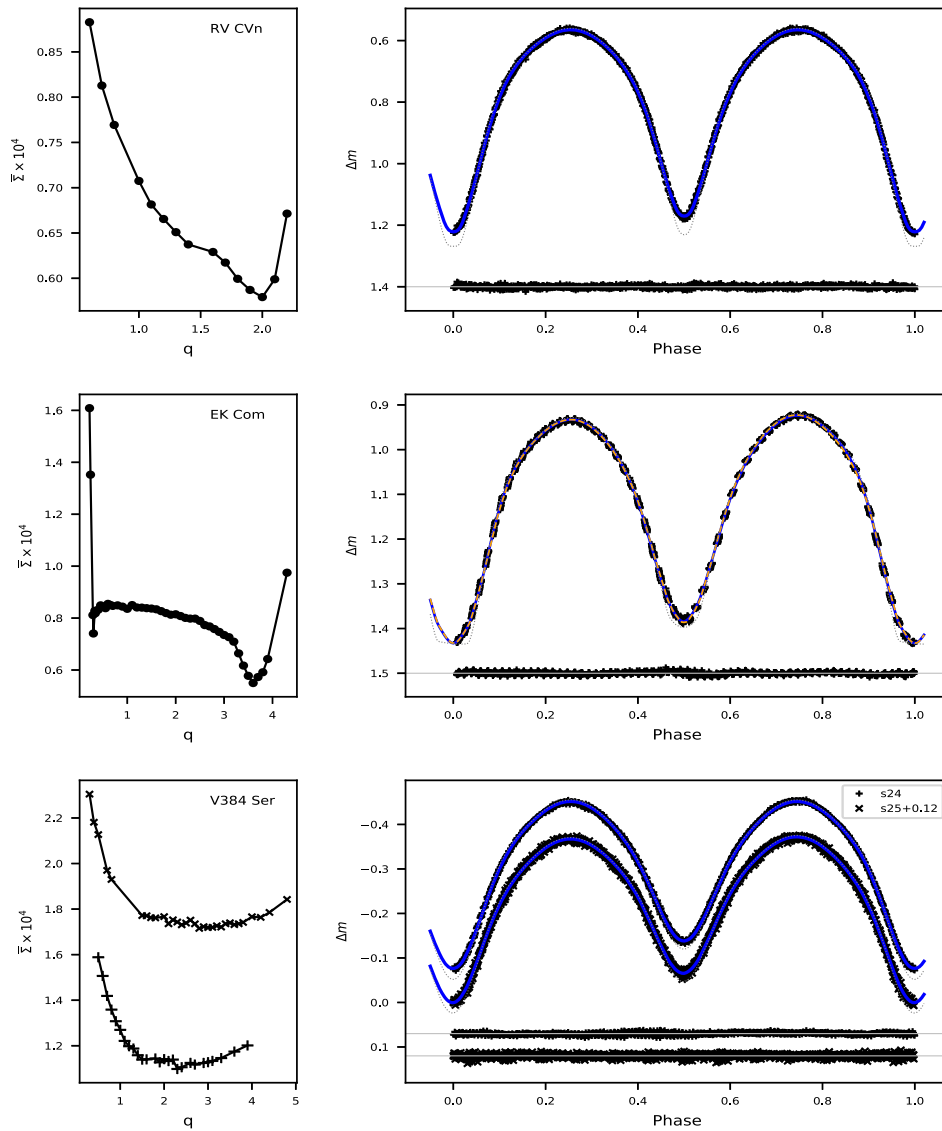
Figure 2. The q–$\overline{\Sigma}$ curves (left panels) and phased light curves (right panels) for RV CVn, EK Com, and V384 Ser. The target names are listed in the left panels. In the right panels, the symbols and thick blue solid lines denote the observed and synthetic (best solutions) light curves, while the thin gray dotted lines represent the theoretical light curves without a smear effect. In the middle right panel, the calculated curve from optional results is shown by the orange dashed line. The residuals of the light curves are shown at the bottom of each panel. The label "s" denotes the TESS sector.

($1/q = 0.575$) and 0.93, respectively, which results in conclusions of W and A subtype, respectively. Therefore, it is important to have another check from new data.

To derive independent photometric solutions for this target, the temperature of star 1 (the star eclipsed at the deeper minimum) was estimated and fixed at 4850 K according to the recent catalog of Gaia DR2 (Gaia Collaboration et al. 2018). A third light was included in the solutions because there is a close companion in its neighborhood. It is found that RV CVn is a W-subtype CB with a mass ratio of about 1.97. The solutions are similar to those obtained by Liu et al. (2014) in temperature difference ($T_1 - T_2 \sim 140$ K) and the degree of contact ($f = 10\%$), while there is a slight difference in the mass ratios and inclination values. Subsequently, we tried using both mass ratio values to fit the RV data and found that both of them show good fits (see the top left panel of Figure 5). The curves from the result of Liu et al. (2014) even match the data slightly better. Therefore, a more reasonable mass ratio should be $1/q = 0.55^{+0.02}_{-0.04}$. Nevertheless, the absolute physical

parameters were estimated (Table 9) using the newly determined mass ratio result in order to make a comparison here. The result of total luminosity (L_{tot}) turns out to be in good agreement with that calculated from the parallax in Gaia DR2 (L_{G2}; see Table 9). The formulae that were utilized to calculate L_{G2} can be found in Chen et al. (2018).

3.2. EK Com

It is noticed that K-type CBs are more likely to be W-subtype, which means that the component eclipsed at the deeper minimum (namely, star 1) is the hotter but less massive component; thus, star 2 should be more massive and larger. It is probable that star 2 (the primary) is more luminous. Therefore, we set the temperature T_2 fixed hereafter.

Object EK Com is interesting because it exhibits long-term variation in its light curve. Its O'Connell effect changes greatly over a long time (Tavakkoli et al. 2017). The light curves from Samec et al. (1996) and Deb et al. (2010) also vary in the depths of minimum light. Those from the former show a typical
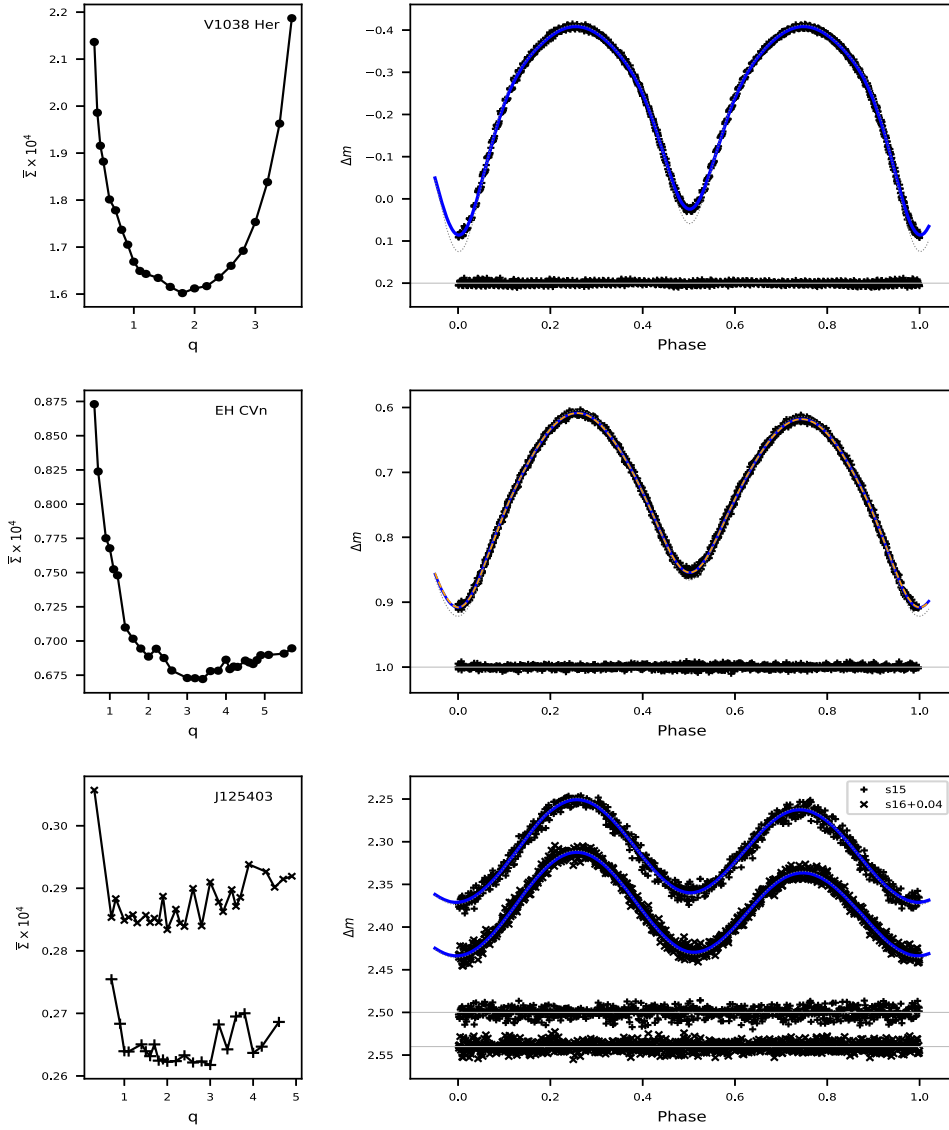
Figure 3. Same as Figure 2 but for V1038 Her, EH CVn, and J125403.

W-subtype feature (deeper occultation), while the latter show more shallow occultation. As mentioned in Section 1, the latter is usually considered to be an A-subtype light curve feature. However, the photometric solution from Deb et al. (2010) actually indicates that the system is W-subtype. Therefore, all photometric solutions until now agree on the W-subtype configuration of the system, while the mass ratio value varies from 2.89 ($1/q = 0.346$; Deb et al. 2010) to 3.5 (Tavakkoli et al. 2017). No spectroscopic mass ratio has yet been obtained.

According to LAMOST DR7, EK Com has a spectral type of G9/G8. To derive the photometric solution, T_2 was estimated to be 5000 K based on LAMOST and Gaia DR2. There is a small asymmetry (the O'Connell effect) in the light curve (see the middle panel of Figure 2). Therefore, a starspot was included when searching for the final solutions. We tried both cool- and hot-spot models, and the solutions are shown in Table 2. Both cases turned out to give good fitting results. The solution with a hot spot has a smaller residual, which means it is more reasonable to adopt. The calculated light curves with the smear effect removed are also displayed in Figure 2. The flat occultation feature of the light curve is excellently recovered.

For the spectroscopic part, except for APOGEE, we also got spectra from the Thai National Observatory (TNO) for EK Com. The observations were made in 2017 with the Middle Resolution ($R \sim 18,000$) fiber-fed Echelle Spectrograph (MRES) mounted on the 2.4 m Ritchey–Chrétien telescope of TNO, which is operated by the National Astronomical Research Institute of Thailand. Some information is listed in Table 6, together with the determined RVs. To test the photometric solutions, parameters from both cool- and hot-spot solutions were used to fit the collected RV data. It is found that both inputs lead to good fits (see the middle left panel of Figure 5). From the RV fit, both sets of solutions should be acceptable. Both of them agree that the system is a W-subtype CB with a small mass ratio ($1/q \sim 0.3$) and a high inclination ($i \gtrsim 85$), which is in accord with the results from the literature (see Samec et al. 1996; Tavakkoli et al. 2017). It should be noted that different photometric solutions indicate that the light curve alone is not yet able to well constrain the spot configuration. The absolute dimensions were derived and listed in Table 9 (orbital parameters from the hot-spot model were used).

Table 2
Photometric Solutions for the TESS Light Curves of Variables (I)

Parameters	RV CVn		V384 Ser			EK Com		
	qser	free	qser (s24)	el3 (s24)	spot (s25)	qser	cool spot	hot spot
q (M_2/M_1)	2.0	1.971(5)	2.3	1.993(9)	1.355(3)	3.6	3.260(13)	3.637(4)
Ω_{in}	5.2517	5.2103	5.6709	5.2423	4.3065	7.3997	6.9581	7.4476
Ω_{out}	4.6545	4.6140	5.0655	4.6453	3.7370	6.7731	6.3355	6.8205
T_1 (K)	4850[a]	4850[a]	5033(2)	5043(5)	5010(8)	5240(3)	5279(4)	5354(8)
T_2 (K)	4706(1)	4703(2)	4750[a]	4750[a]	4750[a]	5000[a]	5000[a]	5000[a]
i (deg)	84.05(4)	84.16(15)	67.92(3)	69.71(10)	68.55(13)	83.62(10)	87.50(19)	84.22(9)
L_1/L_{total} (%)	37.85(2)	37.97(11)	37.42(3)	36.64(20)	44.2(2)	27.59(3)	28.23(26)	28.93(8)
L_3/L_{total} (%)	...	0.71(26)	...	10.2(4)	9.3(7)	...	6.5(7)	0.81(13)
$\Omega_1 = \Omega_2$	5.196(1)	5.152(8)	5.658(1)	5.207(11)	4.292(6)	7.328(2)	6.848(6)	7.365(5)
f (%)	9.4(2)	9.8(1.3)	2.2(2)	5.9(1.8)	2.5(1.0)	11.4(4)	17.6(1.0)	13.1(3)
r_1 (pole)	0.3046(1)	0.3061(3)	0.2899(1)	0.3031(2)	0.3326(3)	0.2601(2)	0.2702(2)	0.2601(1)
r_1 (side)	0.3187(2)	0.3202(4)	0.3025(1)	0.3168(2)	0.3484(4)	0.2714(2)	0.2824(3)	0.2714(2)
r_1 (back)	0.3544(2)	0.3561(5)	0.3358(2)	0.3513(3)	0.3810(5)	0.3077(3)	0.3210(4)	0.3083(3)
r_2 (pole)	0.4190(1)	0.4180(9)	0.4269(1)	0.4170(3)	0.3831(8)	0.4662(2)	0.4611(2)	0.4676(3)
r_2 (side)	0.4460(2)	0.4449(11)	0.4549(1)	0.4435(4)	0.4043(10)	0.5033(2)	0.4972(3)	0.5052(5)
r_2 (back)	0.4759(2)	0.4750(16)	0.4825(2)	0.4726(5)	0.4348(14)	0.5294(2)	0.5248(3)	0.5314(6)
θ_s (deg)	...	...	...	...	28.7[b]	...	131.8[b]	28.6[b]
ψ_s (deg)	...	...	...	...	160(2)	...	69(15)	207.9(1.4)
r_s (deg)	...	...	...	...	13.2(5)	...	11.1(4)	11.4(3)
T_s/T_*	...	...	...	...	0.80[b]	...	0.80[b]	1.28[b]
On star	...	...	...	...	2	...	2	2
$\overline{\Sigma} \times 10^4$	0.5792	0.5776	1.0980	1.0918	1.7222	0.5499	0.3885	0.3312

Notes. qser: from q-search method.
[a] Assumed. $L_{total} = L_1 + L_2 + L_3$.
[b] Trial; the parameter was fixed at a series of trial values in the calculation until the best value was found. An "s" inside the parentheses in the column head refers to the TESS sector.

Table 3
Photometric Solutions for the TESS Light Curves of Variables (II)

Parameters	V1038 Her		EH CVn			J125403		
	qser	el3	qser	case 1	case 2	qser (s16)	spot (s15)	spot (s16)
q (M_2/M_1)	1.8	1.612(5)	3.4	1.383(3)	1.816(2)	3.0	2.583(21)	3.139(21)
Ω_{in}	4.9661	4.6916	7.1409	4.3499	4.9882	6.6163	6.0585	6.7998
Ω_{out}	4.3757	4.1089	6.5165	3.7787	4.3973	5.9974	5.4468	6.1788
T_1 (K)	4934(2)	4942(3)	5222(6)	4948(8)	5115(6)	5202(28)	5259(78)	5204(55)
T_2 (K)	4750	4750	4750	4750	4750	4750	4750	4750
i (deg)	74.11(4)	75.51(15)	61.24(7)	62.22(6)	60.72(4)	45.6(6)	45.1(1.1)	44.7(9)
L_1/L_{total} (%)	40.8(1)	40.6(3)	33.5(1)	47.1(2)	44.5(1)	35.1(3)	39.3(9)	34.5(6)
L_3/L_{total} (%)	...	6.5(6)	...	...	...	...	...	...
$\Omega_1 = \Omega_2$	4.953(1)	4.662(8)	6.987(3)	4.273(4)	4.902(2)	6.578(11)	6.010(25)	6.707(25)
f (%)	2.3(2)	5.1(1.4)	24.6(5)	13.4(6)	14.5(4)	6.2(1.8)	8.0(4.2)	14.9(4.0)
r_1 (pole)	0.3093(1)	0.3198(4)	0.2699(2)	0.3375(2)	0.3154(2)	0.2715(8)	0.2837(1)	0.2719(16)
r_1 (side)	0.3232(1)	0.3347(5)	0.2825(2)	0.3546(2)	0.3306(2)	0.2832(9)	0.2963(1)	0.2840(19)
r_1 (back)	0.3563(2)	0.3686(6)	0.3240(4)	0.3913(3)	0.3681(2)	0.3179(15)	0.3316(2)	0.3217(34)
r_2 (pole)	0.4067(1)	0.3990(10)	0.4670(2)	0.3914(6)	0.4139(3)	0.4500(7)	0.4389(2)	0.4571(19)
r_2 (side)	0.4312(1)	0.4226(13)	0.5049(3)	0.4145(7)	0.4404(3)	0.4830(10)	0.4696(3)	0.4921(26)
r_2 (back)	0.4602(2)	0.4529(19)	0.5332(3)	0.4480(11)	0.4722(5)	0.5096(12)	0.4975(4)	0.5197(34)
θ_s (deg)	...	...	...	6[t]	97[t]	...	86[t]	92[t]
ψ_s (deg)	...	...	...	198(1)	312(2)	...	279(8)	295(4)
r_s (deg)	...	...	...	46.4(9)	8.8(2)	...	14.4(5)	15.1(3)
T_s/T_*	...	...	...	1.18[t]	0.60[t]	...	0.90[t]	0.70[t]
On star	...	...	...	1	2	...	2	2
$\overline{\Sigma} \times 10^4$	1.6021	1.5806	0.6722	0.4043	0.4040	0.2618	0.2112	0.1747

3.3. V384 Ser

According to LAMOST DR7, V384 Ser has a spectral type of K2. So far, there are two sets of independent photometric solutions that have recently been reported (Michaels et al. 2019; Zhang et al. 2020). The system was found to be W-subtype, with mass ratios $q = 2.65$ and 3.16 according to Michaels et al. (2019) and Zhang et al. (2020), respectively.

Table 4
Spectroscopy Log from APOGEE and the Newly Determined Velocities

| Targets	UT-MID[a]	HJD[a] (2,400,000+)	EXPTIME[a] (s)	S/N[a]	Phase[b]	V_p (km s^{-1})	V_s (km s^{-1})	V_3 (km s^{-1})
RV CVn	2011-05-22T06:04:56.8	55,703.756507	3194.70	57	0.008	14.2 ± 1.3	⋯	⋯
	2011-05-23T07:05:44.0	55,704.798654	5324.50	84	0.874	-88.2 ± 3.5	205.5 ± 6.5	⋯
	2011-07-17T03:33:02.9	55,759.646863	4792.05	82	0.342	118.8 ± 2.2	-191.3 ± 2.5	⋯
	2012-04-12T09:55:22.1	56,029.918053	2002.04	36	0.954	-49.0 ± 2.0	163.7 ± 3.2	⋯
	2012-05-02T07:14:41.4	56,049.805913	2002.04	50	0.731	-117.1 ± 1.1	240.6 ± 1.4	⋯
	2013-01-23T11:55:18.5	56,315.998511	3503.56	63	0.213	140.7 ± 1.5	-193.6 ± 1.5	⋯
	2018-03-04T09:00:57.2	58,181.879788	2002.04	49	0.001	7.2 ± 1.2	⋯	⋯
	2018-04-04T08:24:35.9	58,212.855093	2502.54	63	0.909	-62.8 ± 2.5	183.61 ± 6.3	⋯
	2018-04-25T06:15:24.3	58,233.765016	3003.05	48	0.477	⋯	-2.9 ± 1.5	⋯
	2018-05-02T05:20:33.1	58,240.726668	2002.04	63	0.302	135.7 ± 1.6	-202.0 ± 1.9	⋯
	2018-05-05T07:25:17.4	58,243.813170	2002.04	59	0.752	-111.1 ± 1.3	245.8 ± 1.8	⋯
	2018-05-24T04:20:28.2	58,262.683816	1001.02	28	0.756	-109.4 ± 1.1	261.1 ± 1.6	⋯
EK Com	2016-04-27T04:04:04.6	57,505.673517	4025.47	127	0.910	-45.6 ± 1.0	⋯	⋯
	2017-05-15T04:43:42.1	57,888.699969	1341.82	76	0.162	50.7 ± 1.7	-284.9 ± 2.5	⋯
	2017-05-16T03:58:38.3	57,889.668602	3631.43	127	0.792	-95.3 ± 3.0	218.3 ± 6.9	⋯
V384 Ser	2018-06-11T07:05:46.6	58,280.799349	4025.47	176	0.324	85.7 ± 5.6	-200.2 ± 7.4	-2.1 ± 0.2
	2018-06-12T03:40:01.1	58,281.656430	1842.33	122	0.513	-21.0 ± 1.0	⋯	-2.3 ± 0.3
V1038 Her	2016-05-07T10:41:58.1	57,515.948889	1341.82	104	0.646	-126.1 ± 1.4	180.3 ± 1.8	-2.6 ± 0.5
	2016-05-08T07:41:14.9	57,516.823405	1341.82	89	0.907	-61.3 ± 4.9	121.3 ± 5.1	-1.2 ± 0.4
	2016-05-09T10:17:35.2	57,517.931995	1341.82	89	0.041	-3.7 ± 0.9	⋯	-1.8 ± 0.6
	2017-06-15T05:50:09.9	57,919.746312	447.27	66	0.342	138.2 ± 1.5	-171.9 ± 1.5	2.0 ± 0.4
	2017-06-16T04:22:22.8	57,920.685336	4579.21	186	0.843	-93.1 ± 3.9	142.6 ± 5.2	-1.4 ± 0.4
EH CVn	2017-04-17T05:39:11.7	57,860.739841	2683.64	69	0.441	-35.0 ± 0.8	⋯	⋯
	2017-04-18T05:14:02.7	57,861.722358	1341.82	52	0.169	63.5 ± 1.0	-229.1 ± 1.2	⋯
J125403	2018-03-05T10:12:23.4	58,182.928935	2002.04	41	0.784	-57.7 ± 1.3	166.4 ± 2.3	⋯
	2018-03-09T10:09:39.3	58,186.927029	2502.54	36	0.658	-26.6 ± 1.2	⋯	⋯
	2018-03-31T07:50:41.8	58,208.830191	2002.04	12	0.144	4.5 ± 3.6	⋯	⋯
	2018-04-03T08:42:30.7	58,211.866085	2002.04	30	0.438	-12.4 ± 0.7	⋯	⋯
	2018-04-07T08:10:23.2	58,215.843660	3003.05	45	0.236	29.1 ± 1.7	-170.6 ± 2.4	⋯
	2018-04-23T06:39:31.7	58,231.779918	1001.02	17	0.523	-17.2 ± 1.3	⋯	⋯

Notes.
[a] Retrieved from apVisit files.
[b] Determined using the following initial ephemerides (HJD) and periods. RV CVn: 2456001.8955 (for MJD 55,703–56,315; Diethelm 2012) and 2457855.4339 (for MJD 58,000+; Pagel 2018), 0.269567 day; EK Com: 2457465.5615 (Hubscher 2017), 0.266685 day; V384 Ser: 2458290.3866 (Pagel 2020), 0.268729 day; V1038 Her: 2457125.57364 (Jurysek et al. 2017), 0.268180 day; EH CVn: 2458172.1786 (Xia et al. 2018), 0.263583 day; J125403: 2458743.16197 (this study), 0.268798 day. The phase for EK Com is half-cycle corrected from Hubscher (2017) to be in phase with its light curve.

Table 5
Spectroscopy Log from LAMOST and the Newly Determined Velocities

Targets	DATE-OBS[a]	HJD[a] (2,400,000+)	EXPTIME[a] (s)	S/N[a] B band	Phase[b]	V_p (km s^{-1})	V_s (km s^{-1})	V_3 (km s^{-1})
V384 Ser	2020-06-07T14:27:27	59,008.106167	1200	17	0.766	-126.3 ± 3.9	197.0 ± 2.8	-14.9 ± 2.0
	2020-06-07T14:50:48	59,008.122381	1200	16	0.826	-123.2 ± 3.1	177.2 ± 2.3	-10.7 ± 1.3
	2020-06-07T15:14:12	59,008.138631	1200	14	0.887	-107.8 ± 5.0	128.4 ± 4.3	-3.6 ± 2.4
EH CVn	2019-03-13T18:08:55	58,556.260475	1200	16	0.157	52.8 ± 1.6	-200.1 ± 1.6	⋯
	2019-03-13T18:32:14	58,556.276668	1200	15	0.219	70.1 ± 2.1	-220.8 ± 2.4	⋯
	2019-03-13T18:55:33	58,556.292861	1200	14	0.280	62.4 ± 1.4	-228.4 ± 1.7	⋯
	2020-04-11T16:23:19	58,951.187253	1200	28	0.459	⋯	-42.9 ± 0.3	⋯
	2020-04-11T16:46:41	58,951.203479	1200	25	0.520	⋯	-38.7 ± 0.7	⋯
	2020-04-11T17:10:04	58,951.219717	1200	29	0.582	-41.6 ± 0.8	⋯	⋯

Notes.
[a] Retrieved from single-exposure spectra.
[b] Determined using the following initial ephemerides (HJD) and periods. V384 Ser: 2458985.59583 (this study), 0.268729 day; EH CVn: 2458172.1786 (Xia et al. 2018), 0.263583 day.
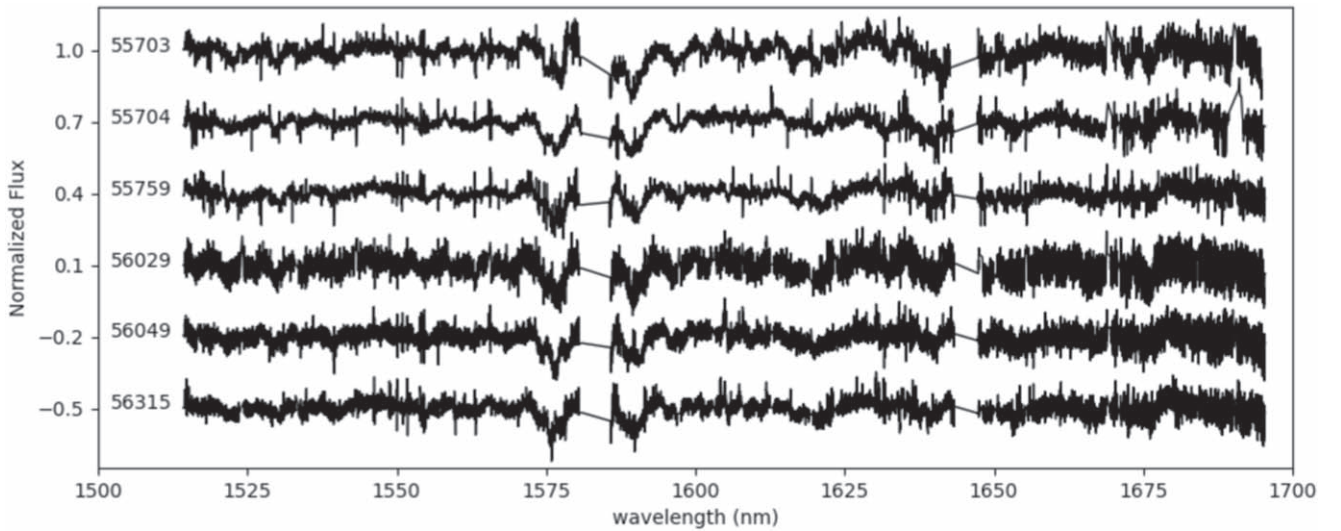
Figure 4. Normalized spectra of RV CVn from APOGEE-1. The spectra are vertically shifted for clarity. The MJD of each spectrum is marked on the left side.

Table 6
Observation of EK Com with MRES and the Newly Determined Velocities

DATE-OBS[*]	HJD (2,400,000+)	EXPTIME (s)	Phase[†]	V_p (km s^{-1})	V_s (km s^{-1})
2017-04-05T18:21:13	57,849.26955	900	0.307	33.3 ± 1.5	-274.8 ± 1.5
2017-04-05T18:38:41	57,849.28168	900	0.352	18.2 ± 1.3	-247.7 ± 1.4
2017-04-05T19:42:35	57,849.32605	900	0.519	-27.2 ± 0.8	⋯
2017-04-05T19:58:01	57,849.33677	900	0.559	⋯	⋯
2017-04-05T21:06:11	57,849.38411	900	0.737	-78.5 ± 1.7	249.0 ± 1.7
2017-04-05T21:21:37	57,849.39483	900	0.777	-79.6 ± 1.7	241.5 ± 1.7

Michaels et al. found a significant luminosity contribution from a third body, while Zhang et al. did not. The former authors further estimated the mass of the tertiary component from the orbital period analysis and speculated that its spectral type is K3 or K4.

TESS observed V384 Ser in sectors 24 and 25 (hereafter s24 and s25). This object was not only observed with FFI images but also recorded in short-cadence mode. However, to be consistent with other targets, the long-cadence light curves (LLCs) were analyzed first. For the light curve from s24, no spots were included in the calculation, since there is no obvious asymmetry, while for s25, the spots were considered because the asymmetry is significant. A significant third light was found, which contributes to ~10% in the TESS band. The mass ratios determined from the LLCs of the two sectors are quite different, while both of them are smaller ($1/q$ is larger) than those found by the previous authors.

The time resolution of the short-cadence light curves (SLCs) of V384 Ser is much higher and thus benefits the analysis of the long-term variation of the light curve. The SLC data of V384 Ser used in this paper can be found in MAST: 10.17909/fpt5-8n40. In Figure 6 (top left panel), we can see that the change of $-\Delta$ Max and $-\Delta$ Min of the light curves is significant and fast. Cycle-to-cycle variation of the light curve is probably true. Four segments of the data selected (labeled as "s24a," "s24b," "s25a," and "s25b") are shown in the bottom left panel. They are each binned into 300 data points. It is seen that even in the same sector, the light curves are quite different. The fast

variation indicates that V384 Ser is an active system, which is the same conclusion obtained by Michaels et al. (2019). Photometric solutions were carried out for s24a and s24b as typical examples (light curves with roughly equal and different maxima, respectively), and the results are shown in Table 7 and the top right panel of Figure 6. Similar to the situation of the LLCs of s24 and s25, we got quite different mass ratios for s24a (no spots) and s24b(with spots). When the spotted scenario was considered for s24a (very slight asymmetry in the light curve), the mass ratio turned out to be close to that of s24b.

To solve the problem of different mass ratios, a simultaneous fitting was carried out for the light curve of s24a and the RV data. These RVs were determined from APOGEE and LAMOST MRS spectra (see Tables 4 and 5). The derived mass ratio from the simultaneous solutions (the "s24a with RV" column of Table 7) is $q \sim 1.74$. Interestingly, this value is very close to the mean result ($q = 1.757$) from the other three solutions. The derived RV curves are shown in Figure 5. The curves from the el3 solutions of s24 ($q = 1.993$) are also plotted for comparison. It is seen that the curves from the simultaneous solutions fit the observation better. Therefore, the corresponding results from "s24a with RV" were adopted, and the absolute dimensions were estimated accordingly.

It is worth mentioning that the spectra of V384 Ser were found to be full of narrow lines overlapped on the broad absorption features (see Figure 7). These narrow lines may come from a tertiary component with slower rotation. As was
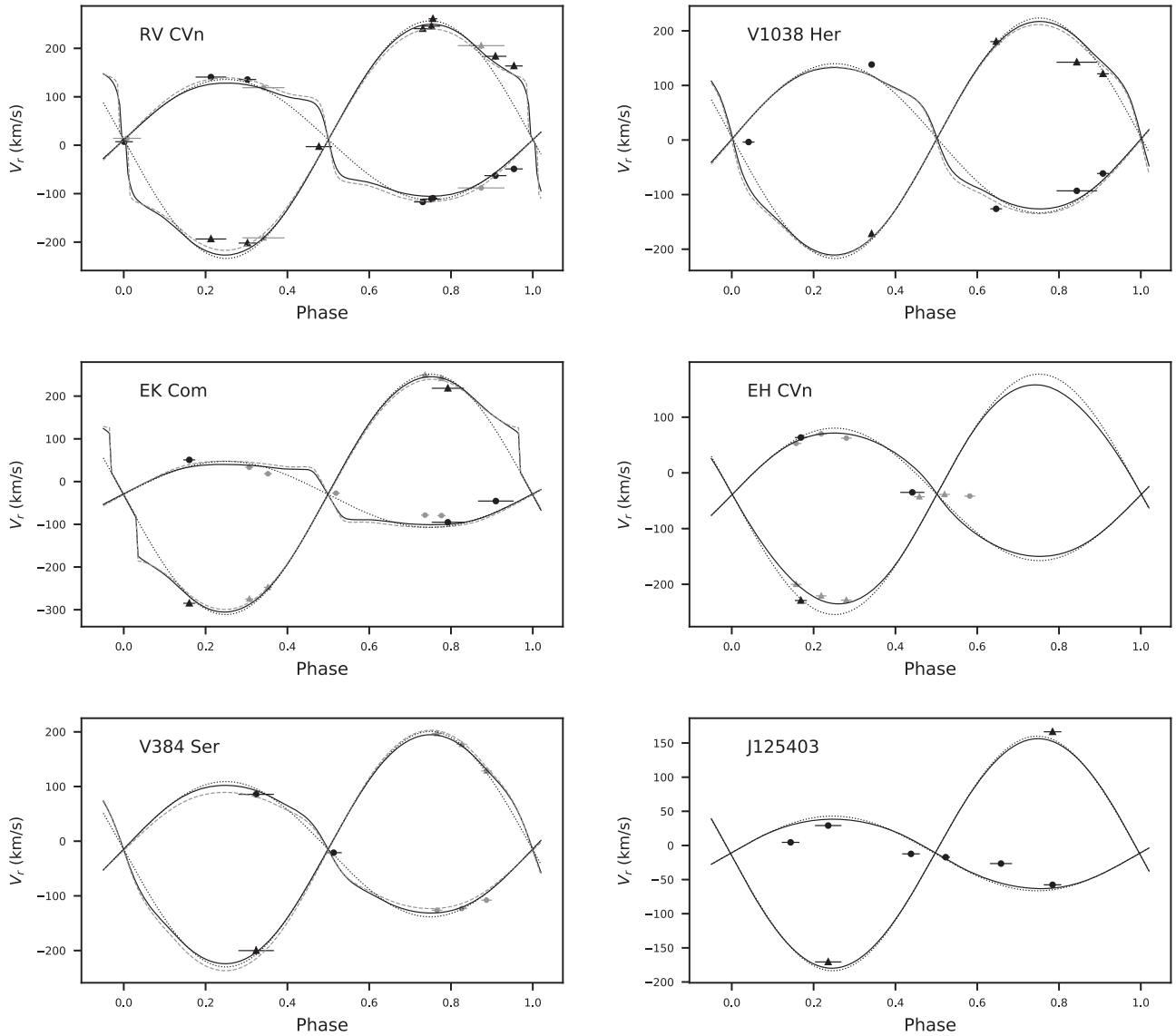
Figure 5. The RVs of the targets and fittings. The filled circles and triangles represent RV observations of primary and secondary components, respectively. Small gray symbols denote data from different sources besides APOGEE-2: APOGEE-1 for RV CVn, TNO for EK Com, and LAMOST for V384 Ser and EH CVn. The dotted lines give the respective point circular orbit (sine-curve) fits, while the solid lines give the RV curves, which are calculated from the best solutions (taking into account the proximity correction) of each object. The dashed lines in a few panels denote solutions from optional results (explained in the text) for comparison. The horizontal bars stand for half the exposure time.

expected, prominent features of a third component were found in the CCFs (see Figure A1), and this is in accordance with the photometric solutions. The determined RVs of the third component were close to that of the binary system (see Table 9). Furthermore, through $O − C$ analysis, the orbital period of V384 Ser is found to show periodic variation (Michaels et al. 2019). Combining all of these factors, V384 Ser is most likely to be a hierarchical triple system. For the luminosity contribution from the tertiary component, our estimation is smaller than Michaels' decision. In fact, the parameters from our solutions are closer to that from "solution 2" of Michaels et al. (2019), except for the mass ratio. This is understandable, since the third light can make the mass ratio more uncertain (Hambálek & Pribulla 2013; Liu 2021). Nevertheless, the spectroscopic analysis confirms the results from our TESS photometry. Combining photometric solutions and the spectroscopic analysis, the luminosity of the tertiary component was roughly estimated to be 0.058 $L_\odot$, which

corresponds to ~ 0.5 $M_\odot$ (estimated from Eker et al. 2018 and Mann et al. 2019) for a main-sequence star. If the mass function from Michaels et al. (2019) was well determined, the orbital inclination of the companion should be significantly higher than 45° ($i_3 \sim 70°$).

3.4. V1038 Her

Except for a few observed minimum light times (e.g., Brat et al. 2011; Karampotsiou et al. 2016; Hubscher 2017), V1038 Her has no photometric solutions published yet. The spectral type from the LAMOST low-resolution survey (LRS) is K3. Through TESS photometry, the photometric solutions were derived for the first time. A third light contributing to $\sim 6.5\%$ in the TESS band was found, and the mass ratio was found to be larger ($1/q \sim 0.62$) than other targets. In addition to the TESS light curve, we also got light curves from the American Association of Variable Star Observers (AAVSO) in the B, V,
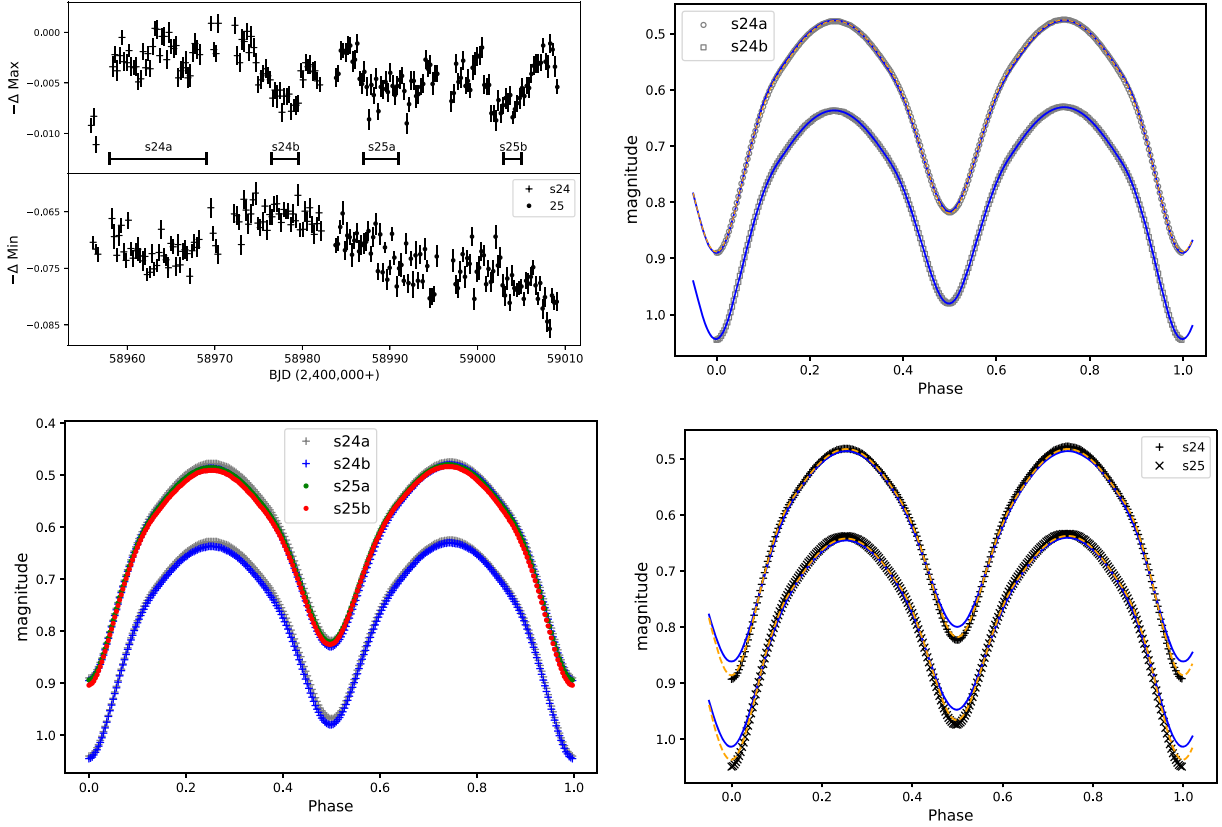
Figure 6. Analysis of the TESS SLCs of V384 Ser. Top left: variation of the light curves indicated from $-\Delta$ Max and $-\Delta$ Min. Bottom left: comparison of light curves of different segments. Top right: observed and calculated light curves. Bottom right: SLCs and fittings from the results of LLCs. The blue solid lines represent theoretical light curves, while the orange dashed lines denote calculated light curves without a smear effect. Except for the top left panel, all light curves shown are rebinned from the original data. The light curves are vertically shifted for clarity.

Table 7
Photometric Solutions for the SLCs of V384 Ser

Parameters	s24a el3	s24a Spot	s24b Spot	s24a with RV
q (M_2/M_1)	2.339(1)	1.533(1)	1.399(1)	1.740(17)
Ω_{in}	5.7246	4.5757	4.3749	4.8791
Ω_{out}	5.1182	3.9966	3.8028	4.2910
T_1 (K)	5050(2)	5004(4)	5002(3)	5062(31)
T_2^a (K)	4750	4750	4750	4750
i (deg)	69.90(6)	69.53(5)	69.67(4)	69.6(5)
L_1/L_{total} (%)	34.5(1)	41.4(1)	42.9(1)	40.2(1.0)
L_3/L_{total} (%)	8.0(3)	9.7(2)	10.4(2)	9.1(2.3)
$\Omega_1 = \Omega_2$	5.685(2)	4.551(1)	4.348(1)	4.848(20)
f (%)	6.6(3)	4.3(2)	4.8(2)	5.4(3.4)
r_1 (pole)	0.2908(1)	0.3234(1)	0.3312(1)	0.3137(13)
r_1 (side)	0.3037(1)	0.3386(1)	0.3471(1)	0.3282(15)
r_1 (back)	0.3385(2)	0.3721(2)	0.3806(1)	0.3623(23)
r_2 (pole)	0.4303(2)	0.3945(2)	0.3871(2)	0.4055(24)
r_2 (side)	0.4592(2)	0.4174(2)	0.4091(2)	0.4301(30)
r_2 (back)	0.4875(3)	0.4477(3)	0.4400(3)	0.4600(43)
θ_s (deg)	...	34^t	11^t	...
ψ_s (deg)	...	172(1)	125(3)	...
r_s (deg)	...	9.8(2)	14.7(2)	...
T_s/T_*	...	0.80^a	0.80^a	...
On star	...	2	2	...
$\Sigma \times 10^4$	0.4923	0.3013	0.2543	6.9101

and Ic bands (see Figure 8), which were observed by Kevin Alton with a QSI 683 wsg-8 CCD camera at the privately owned UnderOak Observatory. According to Kevin Alton, the
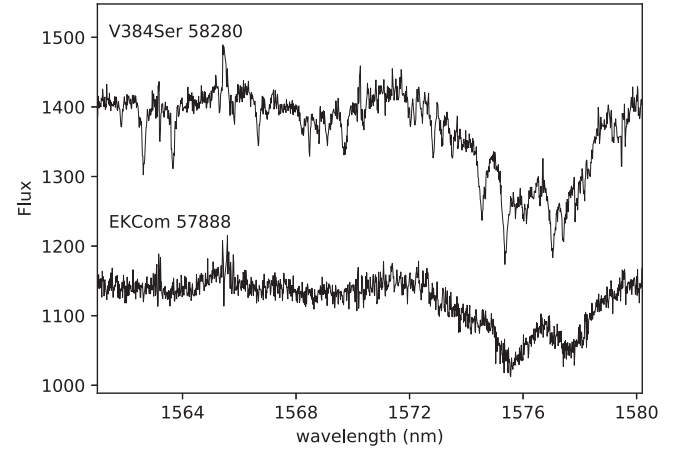
Figure 7. Spectra of V384 Ser and EK Com (a zoomed-in view) from APOGEE. The lower spectrum is vertically shifted. The MJDs of the spectra are listed on the left.

exposure time for the B and Ic passbands was 120 s, while that for V was 105 s. The photometric solutions were derived independently, following the same process. The results are listed in Table 8, and the calculated light curves are shown in Figure 8. The solutions from the TESS and AAVSO light curves are generally in good agreement.

The RVs were fitted with both parameters from the two sets of solutions. No significant difference was seen between the two fittings (see Figure 5). Therefore, the reasonable
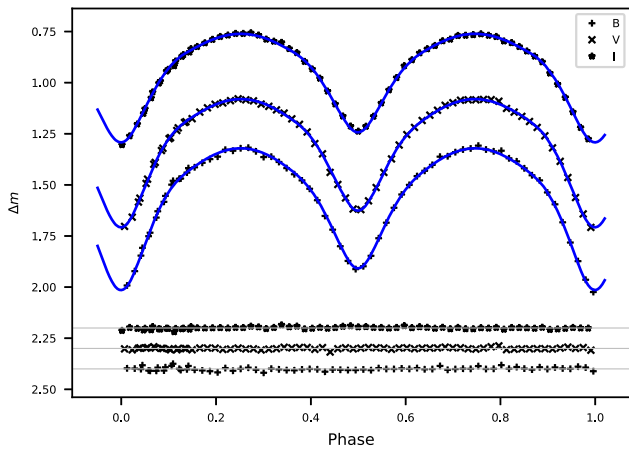
Figure 8. Multiband light curves of V1038 Her and the theoretical fittings.

Table 8
Photometric Solutions for the Multiband Light Curves of V1038 Her

Parameters	Values
$q \ (M_2/M_1)$	1.544(6)
Ω_{in}	4.5914
Ω_{out}	4.0118
$T_2 - T_1$ (K)	−138(5)
i (deg)	76.85(19)
L_1/L_{total} (B) (%)	45.0(4)
L_1/L_{total} (V) (%)	42.7(4)
L_1/L_{total} (Ic) (%)	38.7(4)
L_3/L_{total} (B) (%)	1.7(13)
L_3/L_{total} (V) (%)	4.4(10)
L_3/L_{total} (Ic) (%)	10.2(7)
$\Omega_1 = \Omega_2$	4.558(7)
f (%)	5.8(12)
$\overline{\Sigma} \times 10^4$	1.1954

parameters to adopt for V1038 Her should be $q = 0.634 \pm 0.014$ and $i = 76.1 \pm 0.6$. The temperature is clearly different between the two sets of solutions, which may indicate that this target is active. However, this is not conclusive until there are more observations and evidence.

3.5. EH CVn

The first photometric solutions of EH CVn were derived by Xia et al. (2018), who found the target to be a W-subtype shallow CB based on ground-based observation data. They obtained a small mass ratio of about $1/q \sim 0.30$. No RVs were published.

We tried to revisit EH CVn with TESS photometry and RV study. The result was interesting, in that the mass ratios from the q-search and free calculation process were quite different. The q-search calculation led to a mass ratio of about 3.4, which is very similar to that obtained by Xia et al. (2018), while the free calculation got a much smaller mass ratio q. The spots were added in the final solutions for the asymmetry in the light curve. The final solutions listed in Table 3 were calculated from two cases. For case 1, the latitude of the spot is not constrained, which got a pole spot solution. For case 2, the latitude of the spot is constrained in the low-latitude region. Both solutions led to good fits for the light curve (see Figure 3), of which the mass ratios are significantly different.

The RVs would provide independent evidence for the mass ratio. It comes out that only with the parameters from case 2 can a good fit be obtained. Therefore, the large mass ratio $(1/q = 1.383)$ solution was abandoned, and the intermediate mass ratio was adopted for the target. For other parameters, our solutions are similar to those of Xia et al. (2018). No significant third light was detected in spectra or photometric solutions.

3.6. J125403

Object J125403 was first found to be a periodic variable by Drake et al. (2014). The EW-type shape of the light curve, together with a period of about 0.27 day, indicates that it is a CB candidate. To clarify the nature of this newly discovered eclipsing binary, photometric solutions were searched for the light curves from TESS sectors 15 and 16 (hereafter s15 and s16). However, the low amplitude and variable light curves make the solutions not well determined in spots. Therefore, the results are in fact the mean solutions for the light curve of each sector. The q-search diagrams both show a flat bottom and rugged shape, which means the mass ratio values may not be well constrained. Nevertheless, the photometric solutions from the two sectors are similar in the parameters, though slightly different in the mass ratios.

The parameters from the s16 solution were adopted in the RV fit, which was proved to work well. No significant third light was found in spectra (CCFs) or photometric solutions. However, a small amount of third light is not yet rejected because, photometrically, the orbital inclination is quite low, and spectroscopically, the signal-to-noise ratio (S/N) is not high, which makes the CCFs a bit low-quality. Nevertheless, the W-subtype configuration is undoubtedly confirmed. The masses of the components determined from the joint analysis are quite small compared with other targets, which makes it an interesting object similar to BH Cas (Zoła et al. 2001).

4. Summary and Discussion

The A- and W-subtype classification is a widely accepted concept in defining and describing late-type binaries due to their distinct distribution in mass ratio and effective temperature (see, e.g., Yakut & Eggleton 2005; Latković et al. 2021). It has become an unavoidable topic in the study of W UMa binaries, especially in tracing their evolutionary routes and status (see, e.g., Li et al. 2008; Yildiz & Doğan 2013). However, the detailed model of W UMa binaries is under debate (e.g., Stępień 2009), even for the mechanism of the two subtypes (see Zhang et al. 2020; Song et al. 2020). The K-type CBs are essential for the study of the A/W-subtype problem, since they have the shortest orbital periods among W UMa binaries. The W-subtype phenomenon of K-type CBs is so special among late-type binaries that it might provide key clues for understanding the A- and W-subtype nature and thus the structure and evolution of W UMa binaries.

4.1. W-subtype CB Systems

The RVs were determined for the first time for six selected early K-type targets using spectroscopic data mainly from APOGEE and LAMOST. The RV data were utilized to check the photometric solutions of these targets. The light curves used are mainly from TESS and of high precision. In order to make a comparative study, the photometric solutions were initially derived independently and then checked in the fitting of RVs. It

is proved that all of the selected targets are W-subtype shallow CBs, which were selected independent of subtypes. It is hardly a coincidence. We tried to collect all K-type CBs (period >0.215 day) with both photometric and spectroscopic measurements. Their parameters are listed in Table 10, together with our newly determined ones. Altogether, there are 24 objects, which are arranged in three parts (by the horizontal lines) in the table. Except for the middle part, which contains the six newly confirmed W-subtype systems from this paper, the others are briefly described as follows.

In the first (upper) part, all targets are W-subtype systems. There are three binaries—i Boo, BH Cas, and AH Vir—to mention. Object i Boo is a special object that got an A-subtype solution first but was later confirmed by Lu et al. (2001) to be a W-subtype. This target was found in a triple system (Hill et al. 1989). At a small distance (parallax ∼80 mas) from our Sun, it is very bright. And the tertiary component becomes a visual companion at a separation of about 1″7. This companion (i Boo A) is, however, brighter than the binary member (i Boo B) and hard to exclude in observations; thus, it may affect the photometric solutions. The orbital periods of BH Cas and AH Vir are much longer than those of other K-type CBs listed. For BH Cas, the spectral type was speculated to be K4 and F8 (Metcalfe 1999; Zoła et al. 2001) successively and finally determined to be K3V+G8V by Liu et al. (2019). The absolute parameters of BH Cas were found to be pretty small compared with those of other binaries, while for AH Vir, the total mass is much larger. Nevertheless, all systems (in this part) are confirmed W-subtype CBs.

The lower part contains four exceptions. Among them, OT Cnc (cross ID GSC 1387–0475) and J0930B belong to a special situation in which the temperature difference between the two components is quite small, close to their errors. Therefore, the A/W classifications become meaningless for them, according to the definition. They are labeled "A/W" in the table to refer to those with almost identical temperatures for the two binary components. Object VZ Psc may belong to another situation. It was considered a member of a small subgroup of CBs referred to as the B subtype (Lucy & Wilson 1979; Maceroni et al. 1990), which show a large surface temperature difference between two component stars. Although it has almost the same period and similar shape of light curves, this object was finally found more favorable of a near contact configuration with a fill-out factor of $-5\% \pm 9\%$ (Hrivnak et al. 1995). The last "exception" listed is V345 Gem. Although it has a period of only ∼0.27 day, the effective temperature of the primary is over 6000 K, which is obviously not K-type. Therefore, it is not an exception for the W-subtype phenomenon of K-type CBs.

From the above analysis, we found that there is not even one sample in Table 10 that really belongs to the A subtype. Therefore, it is concluded that almost all of the K-type CBs might be in W-subtype configuration, except for a few systems that have identical temperatures for their components and thus are not necessarily classified as W- or A-subtype according to the original definition. The difference between the primary and secondary components $(T_p - T_s)$ is usually a few hundred kelvins (negative values). A few samples (labeled as "A/W") have a positive temperature difference that is rather small (usually dozens of kelvins). The word "almost" is used because we lack sufficient K-type CBs. Although the samples from Table 10 cover many situations, including a large period range,

low orbital inclinations, and relatively small mass ratios, many cases are not yet covered, such as extremely low mass ratios $(M_s/M_p < 0.15)$, very low inclinations $(i < 40)$, ultrashort periods below the cutoff (∼0.22 day), and systems with evolved components (e.g., BH Cas; Zoła et al. 2001). More observations are necessary in the future, especially spectroscopic observations for RV determination, though recent studies from photometric data alone have already found many late-type CBs (with periods close to the cutoff) overwhelmingly in the W subtype (Li et al. 2019, 2020; Latković & Čeki 2021).

4.2. Additional Comments

Three of our targets are possible triple systems, among which V384 Ser and RV CVn are quite certain. For V384 Ser, the spectra (CCFs) proved the existence of a tertiary component. The contribution of the third light matches the photometric solutions quite well, and it is also consistent with the third-body calculation deduced by the $O-C$ diagram of the orbital period study (Michaels et al. 2019). Therefore, this target is very likely a hierarchical triple system. For RV CVn, a close companion (2MASS J13401740+2818208) is only ∼10″ away and about 1% as bright as RV CVn. With a nearly identical distance (parallax $= 2.37 \pm 0.16$ mas according to Gaia DR2; Gaia Collaboration et al. 2018; Luri et al. 2018) and very similar proper motions ((−6.32, −7.42) mas yr^{-1} for RV CVn and (−6.31, −7.01) mas yr^{-1} for the companion), this visual companion is likely to be a physical one. Another possible triple system is V1038 Her, which is supported by both photometric solutions and the spectroscopic study, which are in good agreement. For the other three targets, no distinctive third lights are detected in their photometric solutions or the spectroscopic study. So, the detection rate of a third light in our samples is similar to that of other CBs collected in Table 10 (nine in 18 samples).

Finally, the physical parameters of the targets listed in Table 9 are still roughly determined values based on the following factors. First, the spectroscopic observations for these targets are not numerous enough, and the phase coverage is not ideal either, which is the reason that the mass ratio cannot be determined with spectra alone and should be determined photometrically in the beginning. The typical errors of the mass ratios of our targets are thereby relatively large, about 0.03–0.05 $(1/q)$ (this will not change the W/A-subtype results). Second, the orbital inclinations are from the photometric solutions, which are correlated with the lengths of the semimajor axis and thus affect the absolute parameters. Nevertheless, the orbital inclinations are usually well constrained by the light curves. Therefore, the uncertainties in the inclinations only moderately increase the errors of the physical parameters. Third, there might be various sources of systematic errors, including (but not limited to) the smear effect of LLCs, the long exposure time of the spectroscopic data, and the single broadband photometry. In all, the real uncertainties should be larger than the standard errors listed in Table 9, which are only based on the fitting. Since the uncertainties of the absolute parameters are huge, they should be of limited use. For the last column, L_{G2} values are calculated using the magnitudes in V from the database and the distance based on Gaia DR2. Taking into account the various errors involved, the total luminosities are generally in agreement with luminosities based on Gaia DR2.

Table 9
RV Fits and Absolute Elements of the Targets

Objects	V_0 (km s^{-1})	A	$(M_1 + M_2)\sin^3 i$	M_1	M_2	R_1	R_2	L_2	$L_{\rm tot}$	$L_{\rm G2}$
RV CVn	12(3)	1.98(4)	1.41(8)	0.48(3)	0.95(6)	0.65(3)	0.89(3)	0.34(1)	0.55(2)	0.564(11)
EK Com	−30(9)	1.90(10)	1.28(19)	0.28(4)	1.02(15)	0.53(5)	0.95(9)	0.52(5)	0.73(7)	0.485(10)
V384 Ser	−14.7(5)	1.92(5)	1.09(7)	0.48(3)	0.84(5)	0.65(3)	0.83(3)	0.31(1)	[a]0.61(2)	0.846(13)
EH CVn	−39(4)	2.00(6)	1.02(6)	0.55(5)	1.00(8)	0.68(2)	0.89(3)	0.36(2)	0.64(4)	0.484(8)
J125403	−11(6)	1.71(10)	0.32(5)	0.23(4)	0.71(13)	0.50(3)	0.84(5)	0.32(2)	0.49(4)	0.761(19)
V1038 Her	4(9)	1.95(15)	1.26(26)	0.53(12)	0.86(20)	0.67(5)	0.83(6)	0.31(5)	[a]0.59(9)	0.623(31)

Notes. Parameters without units noted are in units of solar quantities.
[a] Including the luminosity of a third body.

Table 10
Parameters of K-type CBs with Both Photometric and Spectroscopic Measurements

Name	Period (days)	$q_{\rm sp}$	$M\sin^3 i$ ($M_\odot$)	i (deg)	M_p ($M_\odot$)	M_s ($M_\odot$)	T_p (K)	$T_p - T_s$ (K)	f (%)	eL3	A/W	Refs
CC Com	0.2207	0.527	1.083	89.8	0.717	0.377	4200	−100 ± 60	17	...	W	(1), (2)
J1601	0.2265	0.67	...	79.5	0.86	0.57	4500	...	10	...	W	(3)
V523 Cas	0.2337	0.516	1.110	83.1	0.75	0.38	4410	−326 ± 5	16 *	...	W	(4), VIII
RW Com	0.2373	0.471	1.052	74.9	0.80	0.38	4720	−180 ± 20	6.1	...	W	(5), XIV
J1508	0.2601	0.51	...	90	1.07	0.55	4500	...	12	...	W	(3)
IL Cnc	0.2677	0.57	...	73.6	0.90	0.51	4720	−280 ± 20	9	...	W	(6)
i Boo	0.2678	0.487	1.132	72.8	0.98	0.55	5300	265[c]	...	0.40[a]	W (A)	(7), IV
V1167 Her	0.2753	0.662	1.050	71.6	0.74	0.49	4640	−260 ± 30	9.5	0.48 V	W	(5), XIII
VW Cep	0.2783	0.272	0.85	65.0	0.897	0.247	4930	−270 ± 100	...	0.12[a]	W	(8), (9)
XY Leo	0.2841	0.729	1.188	71.1	0.813	0.593	4524	−326 ± 10	8	0.13	W	(10), (11), XII
RW Dor	0.2854	0.68	0.987	76.9	0.64	0.43	4780	−420 ± 200	⋯	...	W	(12), (13)
PY Vir	0.3113	0.773	1.387	68.9	0.964	0.745	4559	−271 ± 136	0	0.08	W	(14), VIII
BH Cas	0.4059	0.475	...	71.7	0.73[b]	0.35	5555	−445 ± 22	22	...	W	(15), (16)
AH Vir	0.4075	0.303	1.754	85.2	1.360	0.412	5300	−480 ± 200	23	Y	W	(17)
RV CVn	0.2696	0.507	1.41	84.2	0.95	0.48	4703	−147 ± 2	9.8	<0.01 T	W	This study
EK Com	0.2667	0.275	1.28	84.2	1.02	0.28	5000	−354 ± 8	13.1	<0.01 T	W	This study
V384 Ser	0.2687	0.575	1.09	69.6	0.84	0.48	4750	−312 ± 31	5.4	0.09 T	W	This study
EH CVn	0.2636	0.551	1.02	60.7	1.00	0.55	4750	−365 ± 6	14.5	...	W	This study
J125403	0.2688	0.319	0.32	44.7	0.71	0.23	4750	−454 ± 55	14.9	...	W	This study
V1038 Her	0.2682	0.620	1.26	75.5	0.86	0.53	4750	−192 ± 3	5.1	0.065 T	W	This study
OT Cnc	0.2178	0.474	0.280	37.6	0.835	0.396	4500	55 ± 40	43	0.365 V	A/W	(18), (19)
J0930B	0.2277	0.397	...	86	0.86	0.341	4700	...	17	Y	A/W	(20), (21)
VZ Psc	0.2612	0.80	0.601	48	0.81	0.65	4500	390 ± 60	−5	...	EB	(22), (23)
V345 Gem	0.2748	0.142	1.054	61.2	1.371	0.195	6200	360 ± 54	11	0.619 V	A	(19)

Notes. J1601 = 1SWASP J160156.04+202821.6; J1508 = 1SWASP J150822.80−054236.9; J0930B = 1SWASP J093010.78+533859.5 B.

References. (1) Köse et al. (2011), (2) Zola et al. (2010), (3) Lohr et al. (2014), (4) Zhang & Zhang (2004), (5) Djurašević et al. (2011), (6) Liu et al. (2020), (7) Hill et al. (1989), (8) Hill (1989), (9) Kaszas et al. (1998), (10) Djurašević et al. (2006), (11) Zola et al. (2010), (12) Hilditch et al. (1992), (13) Marino et al. (2007), (14) Deb & Singh (2011), (15) Zoła et al. (2001), (16) Metcalfe (1999), (17) Lu & Rucinski (1993), (18) Rucinski & Pribulla (2008), (19) Gazeas et al. (2021), (20) Lohr et al. (2015), (21) Koo et al. (2014), (22) Hrivnak et al. (1995), (23) Maceroni et al. (1990), (VIII) Rucinski et al. (2003), (XIV) Pribulla et al. (2009), (IV) Lu et al. (2001), (XIII) Rucinski et al. (2008), (XII) Pribulla et al. (2007).
[a] Calculated.
[b] Estimated.
[c] Averaged value. T: TESS band. Y: a visual companion nearby (<2″).

Liu et al.

Appendix A
The CCF Profiles of the Targets

The CCF profiles of the targets and their multi-Gaussian fittings are shown in Figures A1–A3.
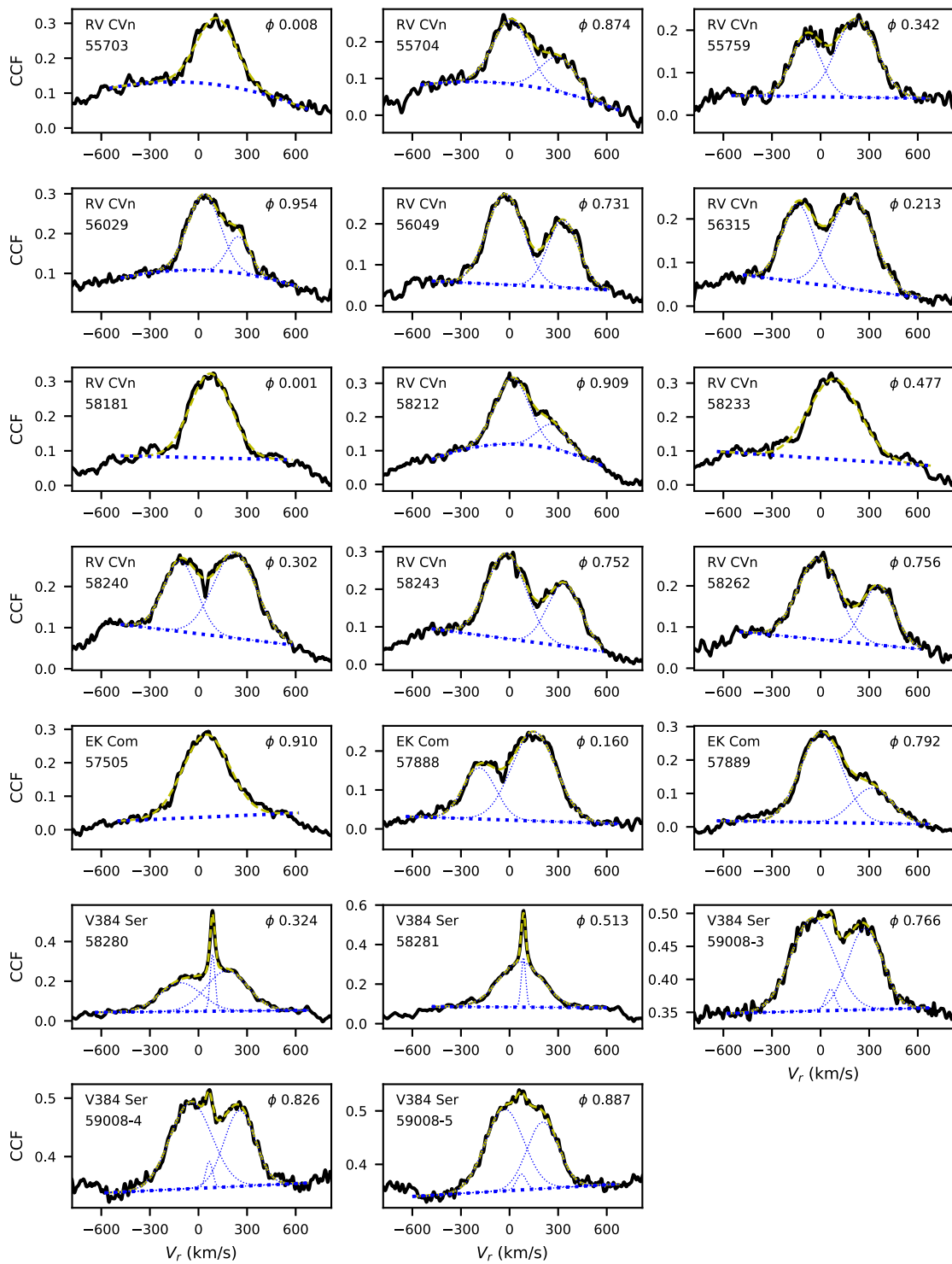
Figure A1. The CCF profiles of the targets and multi-Gaussian fittings for RV CVn, EK Com, and V384 Ser. The multi-Gaussian components are shown with thin blue dotted lines, while the linear or quadratic components are shown with thick blue dotted lines, and the final fitted profiles are shown with yellow dashed lines. The phases are shown in the upper right of each panel.
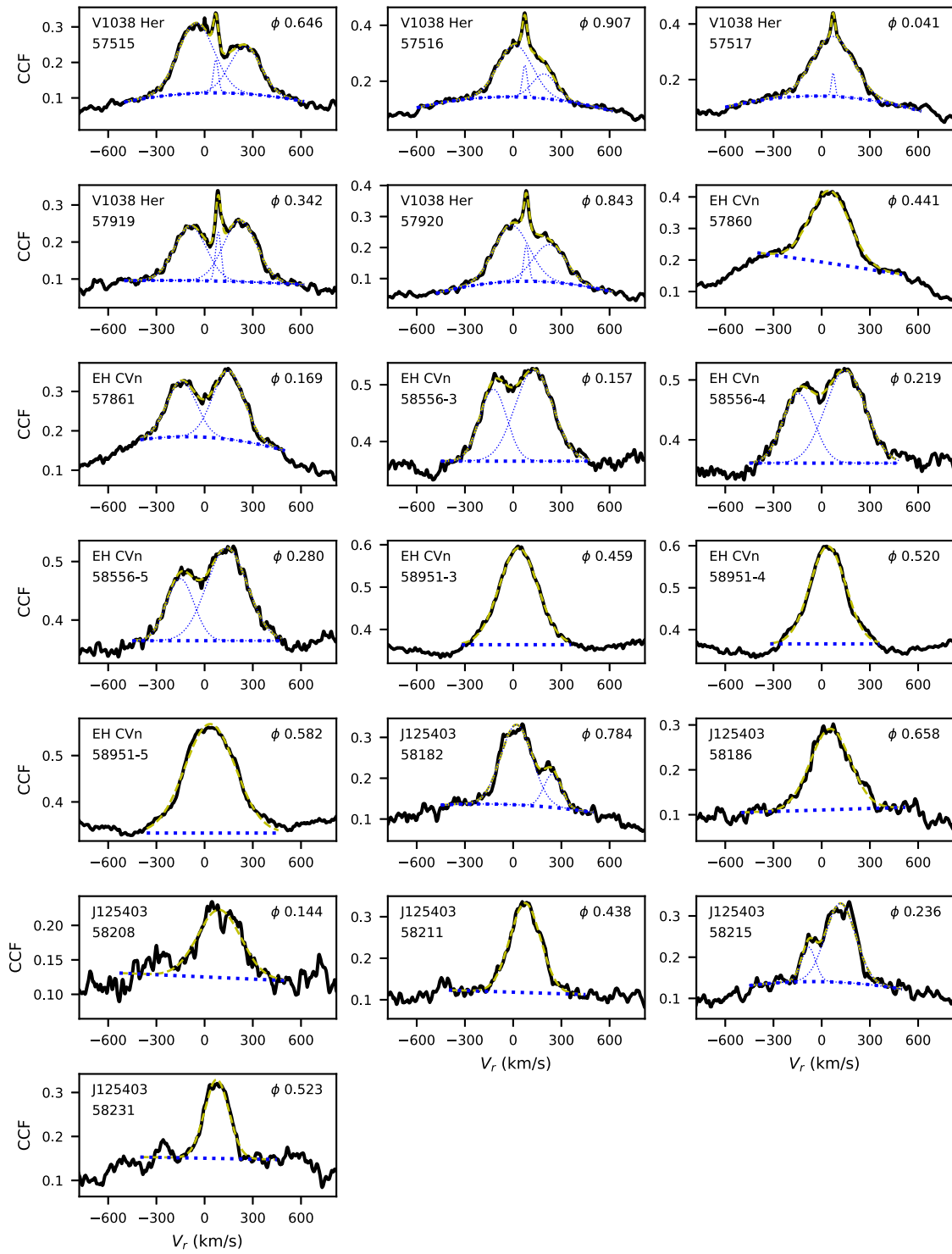
Figure A2. Same as Figure A1 but for V1038 Her, EH CVn, and J125403.
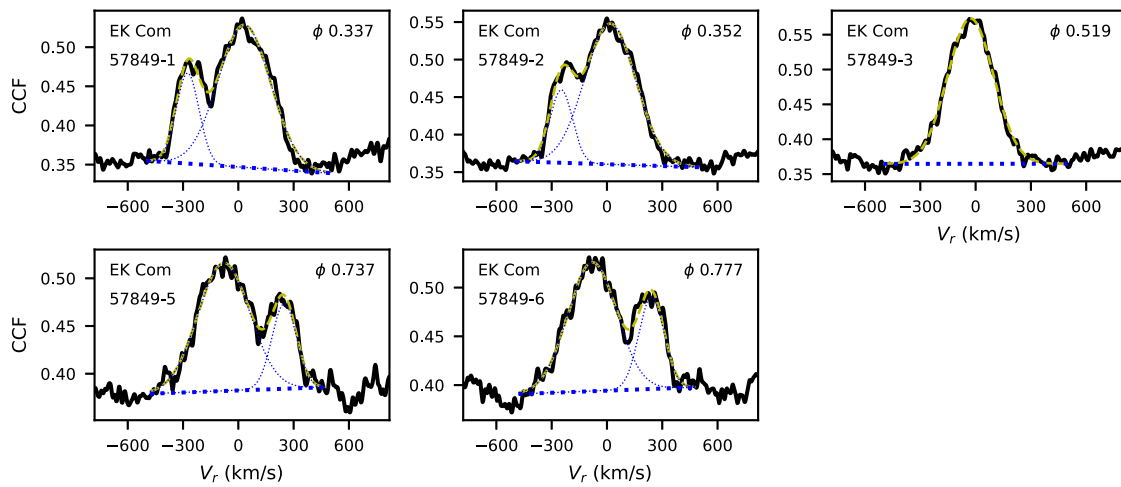
Figure A3. Same as Figure A1 but for EK Com from the observations at TNO.

Appendix B
Newly Determined Minimum Light Times from TESS Data

New minimum light times were determined for the light curves extracted from TESS. Because the data are sparsely sampled for these targets (few data in one cycle), each derived time was determined using the data in a few continuous cycles and thus is an averaged result for these cycles (Liu et al. 2020). The determined times are listed in Table 11 for all targets. In this table, "NA" is the number of data used for determination. The tables will be available in their entirety in machine-readable form.

Table 11
Newly Determined Minimum Light Times

BJD 2,400,000+	Err. (days)	NA	Object
58,929.24999	0.00026	17	RV CVn
58,929.92380	0.00009	16	RV CVn
58,930.05881	0.00018	19	RV CVn
58,930.46299	0.00007	15	RV CVn
58,931.00221	0.00016	19	RV CVn
58,931.13720	0.00017	19	RV CVn
...	...	...	...
58,929.26165	0.00006	16	EK Com
58,929.39510	0.00009	16	EK Com
58,929.92845	0.00009	18	EK Com
...	...	...	...
58,958.05189	0.00009	16	V384 Ser
58,959.12703	0.00019	15	V384 Ser
58,959.26099	0.00011	15	V384 Ser
...	...	...	...
...	...	...	...

(This table is available in its entirety in machine-readable form.)

ORCID iDs

N.-P. Liu ⬤ https://orcid.org/0000-0002-2276-6352
W.-P. Liao ⬤ https://orcid.org/0000-0001-9346-9876
Y. Huang ⬤ https://orcid.org/0000-0003-3250-2876
Z.-L. Yuan ⬤ https://orcid.org/0000-0001-6861-0022

References

Abolfathi, B., Aguado, D. S., Aguilar, G., et al. 2018, ApJS, 235, 42
Alton, K. B., & Stępień, K. 2016, AcA, 66, 357
Alton, K. B., & Stępień, K. 2021, AcA, 71, 123
Astropy Collaboration, Robitaille, T. P., Tollerud, E. J., et al. 2013, A&A, 558, A33
Baran, A., Zola, S., Rucinski, S. M., et al. 2004, AcA, 54, 195
Binnendijk, L. 1970, VA, 12, 217
Blanton, M. R., Bershady, M. A., Abolfathi, B., et al. 2017, AJ, 154, 28
Borkovits, T., Rappaport, S. A., Hajdu, T., et al. 2020, MNRAS, 493, 5005
Borucki, W. J., Koch, D., Basri, G., et al. 2010, Sci, 327, 977
Brasseur, C. E., Phillip, C., Fleming, S. W., et al. 2019, Astrocut: Tools for creating cutouts of TESS images, Astrophysics Source Code Library, ascl:1905.007
Brat, L., Trnka, J., Smelcer, L., et al. 2011, OEJV, 137, 1
Chen, X., Deng, L., de Grijs, R., et al. 2018, ApJ, 859, 140
Clark Cunningham, J. M., Rawls, M. L., Windemuth, D., et al. 2019, AJ, 158, 106
Cui, X.-Q., Zhao, Y.-H., Chu, Y.-Q., et al. 2012, RAA, 12, 1197
Deb, S., & Singh, H. P. 2011, MNRAS, 412, 1787
Deb, S., Singh, H. P., Seshadri, T. R., et al. 2010, NewA, 15, 662
Diethelm, R. 2012, IBVS, 6029, 1
Djurašević, G., Dimitrov, D., Arbutina, B., et al. 2006, PASA, 23, 154
Djurašević, G., Essam, A., Latković, O., et al. 2016, AJ, 152, 57
Djurašević, G., Yılmaz, M., Baştürk, Ö., et al. 2011, A&A, 525, A66
Drake, A. J., Graham, M. J., Djorgovski, S. G., et al. 2014, ApJS, 213, 9
Eggen, O. J. 1967, MmRAS, 70, 111
Eisenstein, D. J., Weinberg, D. H., Agol, E., et al. 2011, AJ, 142, 72
Eker, Z., Bakış, V., Bilir, S., et al. 2018, MNRAS, 479, 5491
Feinstein, A. D., Montet, B. T., Foreman-Mackey, D., et al. 2019, PASP, 131, 094502
Gaia Collaboration, Brown, A. G. A., Vallenari, A., et al. 2018, A&A, 616, A1
Gaia Collaboration, Brown, A. G. A., Vallenari, A., et al. 2021, A&A, 649, A1
Gazeas, K., Zola, S., Liakos, A., et al. 2021, MNRAS, 501, 2897
Guo, D.-F., Li, K., Gao, X., et al. 2020, MNRAS, 497, 3381
Hambálek, L., & Pribulla, T. 2013, CoSka, 43, 27
Hilditch, R. W., Hill, G., & Bell, S. A. 1992, MNRAS, 255, 285
Hill, G. 1989, A&A, 218, 141
Hill, G., Fisher, W. A., & Holmgren, D. 1989, A&A, 211, 81
Hoffmann, M. 1981, IBVS, 1932, 1
Hrivnak, B. J., Guinan, E. F., & Lu, W. 1995, ApJ, 455, 300
Huang, Y., Liu, X.-W., Chen, B.-Q., et al. 2018, AJ, 156, 90
Hubscher, J. 2017, IBVS, 6196, 1
Jayasinghe, T., Stanek, K. Z., Kochanek, C. S., et al. 2020, MNRAS, 493, 4045
Jönsson, H., Holtzman, J. A., Allende Prieto, C., et al. 2020, AJ, 160, 120
Juryšek, J., Hoňková, K., Šmelcer, L., et al. 2017, OEJV, 179, 1
Karampotsiou, E., Gazeas, K., Petropoulou, M., et al. 2016, IBVS, 6158, 1
Kaszas, G., Vinko, J., Szatmary, K., et al. 1998, A&A, 331, 231
Koch, D. G., Borucki, W. J., Basri, G., et al. 2010, ApJL, 713, L79
Koo, J.-R., Lee, J. W., Lee, B.-C., et al. 2014, AJ, 147, 104
Köse, O., Kalomeni, B., Keskin, V., et al. 2011, AN, 332, 626
Larink, J. 1921, AN, 214, 71
Latković, O., & Čeki, A. 2021, PASJ, 73, 132
Latković, O., Čeki, A., & Lazarević, S. 2021, ApJS, 254, 10
Lee, J. W., Kristiansen, M. H., & Hong, K. 2019, AJ, 157, 223
Li, K., Kim, C.-H., Xia, Q.-Q., et al. 2020, AJ, 159, 189
Li, K., Xia, Q.-Q., Kim, C.-H., et al. 2021, AJ, 162, 13
Li, K., Xia, Q.-Q., Michel, R., et al. 2019, MNRAS, 485, 4588
Li, L., Zhang, F., Han, Z., et al. 2008, MNRAS, 387, 97
Lightkurve Collaboration, Cardoso, J. V. d. M., Hedges, C., et al. 2018, Lightkurve: Kepler and TESS time series analysis in Python, Astrophysics Source Code Library, ascl:1812.013
Lindegren, L., Klioner, S. A., Hernández, J., et al. 2021, A&A, 649, A2
Liu, C., Fu, J., Shi, J., et al. 2020, arXiv:2005.07210
Liu, J., Esamdin, A., Zhang, Y., et al. 2019, PASP, 131, 084202
Liu, L. 2021, PASP, 133, 084202
Liu, N., Fu, J.-N., Zong, W., et al. 2019, RAA, 19, 075
Liu, N., Qian, S.-B., & Leung, K.-C. 2014, in ASP Conf. Ser. 482, Tenth Pacific Rim Conference on Stellar Astrophysics, ed. H.-W. Lee, Y. W. Kang, & K.-C. Leung (San Francisco, CA: ASP), 163
Liu, N.-P., Qian, S.-B., Soonthornthum, B., et al. 2014a, AJ, 147, 41
Liu, N.-P., Qian, S.-B., Soonthornthum, B., et al. 2015, AJ, 149, 148
Liu, N.-P., Sarotsakulchai, T., Rattanasoon, S., et al. 2020, PASJ, 72, 73
Lohr, M. E., Hodgkin, S. T., Norton, A. J., et al. 2014, A&A, 563, A34
Lohr, M. E., Norton, A. J., Gillen, E., et al. 2015, A&A, 578, A103
Lu, L.-N., Liu, J.-Z., Jiang, D.-K., et al. 2020, RAA, 20, 196
Lu, W., & Rucinski, S. M. 1999, AJ, 118, 515
Lu, W., Rucinski, S. M., & Ogłoza, W. 2001, AJ, 122, 402
Lu, W.-X., & Rucinski, S. M. 1993, AJ, 106, 361
Lucy, L. B. 1967, ZAp, 65, 89
Lucy, L. B., & Wilson, R. E. 1979, ApJ, 231, 502
Luri, X., Brown, A. G. A., Sarro, L. M., et al. 2018, A&A, 616, A9
Maceroni, C., van Hamme, W., van't Veer, F., et al. 1990, A&A, 234, 177
Majewski, S. R., Schiavon, R. P., Frinchaboy, P. M., et al. 2017, AJ, 154, 94
Majewski, S. R. & APOGEE Team 2016, AN, 337, 863
Mann, A. W., Dupuy, T., Kraus, A. L., et al. 2019, ApJ, 871, 63
Marino, B. F., Walker, W. S. G., Bembrick, C., et al. 2007, PASA, 24, 199
Matijevič, G., Zwitter, T., Munari, U., et al. 2010, AJ, 140, 184
Metcalfe, T. S. 1999, AJ, 117, 2503
Michaels, E. J., Lanning, C. M., & Self, S. N. 2019, JAVSO, 47, 43
Nardiello, D., Borsato, L., Piotto, G., et al. 2019, MNRAS, 490, 3806
Oelkers, R. J., & Stassun, K. G. 2018, AJ, 156, 132
Pagel, L. 2018, IBVS, 6244, 1
Pagel, L. 2020, BAV J., 033, 1
Panchal, A., & Joshi, Y. C. 2021, AJ, 161, 221
Pribulla, T., Rucinski, S. M., Blake, R. M., et al. 2009, AJ, 137, 3655
Pribulla, T., Rucinski, S. M., Conidis, G., et al. 2007, AJ, 133, 1977
Pribulla, T., Rucinski, S. M., DeBond, H., et al. 2009, AJ, 137, 3646
Qian, S.-B., Yang, Y.-G., Soonthornthum, B., et al. 2005, AJ, 130, 224
Qian, S.-B., Zhu, L.-Y., Liu, L., et al. 2020, RAA, 20, 163
Ricker, G. R., Winn, J. N., Vanderspek, R., et al. 2015, JATIS, 1, 014003
Ruciński, S. M. 1969, AcA, 19, 245
Rucinski, S. M. 2002, AJ, 124, 1746
Rucinski, S. M., Capobianco, C. C., Lu, W., et al. 2003, AJ, 125, 3258
Rucinski, S. M., Lu, W., & Mochnacki, S. W. 2000, AJ, 120, 1133
Rucinski, S. M., & Pribulla, T. 2008, MNRAS, 388, 1831
Rucinski, S. M., Pribulla, T., Mochnacki, S. W., et al. 2008, AJ, 136, 586
Samec, R. G., Gray, J. D., & Carrigan, B. J. 1996, Obs, 116, 75
Schilt, J. 1927, ApJ, 65, 124
Song, H., Meynet, G., Maeder, A., et al. 2020, ApJ, 905, 39
Stassun, K. G., Oelkers, R. J., Pepper, J., et al. 2018, AJ, 156, 102
Stępień, K. 2009, MNRAS, 397, 857
Sun, W., Chen, X., Deng, L., et al. 2020, ApJS, 247, 50
Szalai, T., Kiss, L. L., Mészáros, S., et al. 2007, A&A, 465, 943
Tavakkoli, F., Haghi, A., Hosseini, S. M., et al. 2017, NewA, 56, 14
Van Hamme, W., & Wilson, R. E. 2007, ApJ, 661, 1129
Wang, R., Luo, A.-L., Chen, J.-J., et al. 2019, ApJS, 244, 27
Watson, C. L., Henden, A. A., & Price, A. 2006, SASS, 25, 47
Wilson, R. E. 1979, ApJ, 234, 1054
Wilson, R. E. 1994, PASP, 106, 921
Wilson, R. E. 2008, ApJ, 672, 575
Wilson, R. E. 2012, AJ, 144, 73
Wilson, R. E., & Devinney, E. J. 1971, ApJ, 166, 605
Wilson, R. E., Van Hamme, W., & Terrell, D. 2010, ApJ, 723, 1469
Xia, Q.-Q., Li, K., Chen, X., et al. 2018, PASJ, 70, 104
Yakut, K., & Eggleton, P. P. 2005, ApJ, 629, 1055
Yıldız, M. 2014, MNRAS, 437, 185
Yildiz, M., & Doğan, T. 2013, MNRAS, 430, 2029
Zasche, P., Wolf, M., Uhlař, R., et al. 2014, AJ, 147, 130
Zhai, D., & Lu, W. 1989, ChA&A, 13, 350
Zhang, L., Zhu, Z., Yue, Q., et al. 2020, MNRAS, 491, 6065
Zhang, X. B., & Zhang, R. X. 2004, MNRAS, 347, 307
Zhang, X.-D., Qian, S.-B., & Liao, W.-P. 2020, MNRAS, 492, 4112
Zhao, G., Zhao, Y.-H., Chu, Y.-Q., et al. 2012, RAA, 12, 723
Zola, S., Baran, A., Debski, B., et al. 2017, MNRAS, 466, 2488
Zola, S., Gazeas, K., Kreiner, J. M., et al. 2010, MNRAS, 408, 464
Zoła, S., Niarchos, P., Manimanis, V., et al. 2001, A&A, 374, 164
Zong, W., Fu, J.-N., De Cat, P., et al. 2018, ApJS, 238, 30